The MUSE Ultra Deep Field (MUDF). II. Survey design and the gaseous properties of galaxy groups at 0.5 < z < 1.5

M. Fossati [●],[1,2]★ M. Fumagalli [●],[1,2,3] E. K. Lofthouse,[1,2] V. D'Odorico,[4,5] E. Lusso [●],[6,7]
S. Cantalupo [●],[8] R. J. Cooke [●],[1,2] S. Cristiani,[4] F. Haardt,[9,10] S. L. Morris,[2,11]
C. Peroux,[12,13] L. J. Prichard,[14] M. Rafelski,[14,15] I. Smail [●][2] and T. Theuns[1]

[1]*Institute for Computational Cosmology, Durham University, South Road, Durham DH1 3LE, UK*
[2]*Centre for Extragalactic Astronomy, Durham University, South Road, Durham DH1 3LE, UK*
[3]*Dipartimento di Fisica G. Occhialini, Università degli Studi di Milano-Bicocca, Piazza della Scienza 3, I-20126 Milano, Italy*
[4]*INAF, Osservatorio Astronomico di Trieste, Via G. B. Tiepolo 11, I-34143 Trieste, Italy*
[5]*Scuola Normale Superiore, Piazza dei Cavalieri 7, I-56126 Pisa, Italy*
[6]*Dipartimento di Fisica e Astronomia, Università di Firenze, via G. Sansone 1, Sesto Fiorentino, I-50019 Firenze, Italy*
[7]*INAF–Osservatorio Astrofisico di Arcetri, I-50125 Firenze, Italy*
[8]*Department of Physics, ETH Zurich, Wolgang-Pauli-Strasse 27, CH-8093 Zurich, Switzerland*
[9]*DiSAT, Università degli Studi dell'Insubria, Via Valleggio 11, I-22100 Como, Italy*
[10]*INFN, Sezione di Milano-Bicocca, Piazza della Scienza 3, I-20126 Milano, Italy*
[11]*Centre for Advanced Instrumentation, Durham University, South Road, Durham DH1 3LE, UK*
[12]*European Southern Observatory (ESO), Karl-Schwarzschild-Str. 2, D-85748 Garching b. München, Germany*
[13]*Aix Marseille Université, CNRS, LAM (Laboratoire d'Astrophysique de Marseille) UMR 7326, F-13388 Marseille, France*
[14]*Space Telescope Science Institute, 3700 San Martin Drive, Baltimore, MD 21218, USA*
[15]*Department of Physics and Astronomy, Johns Hopkins University, Baltimore, MD 21218, USA*

ABSTRACT

We present the goals, design, and first results of the MUSE Ultra Deep Field (MUDF) survey, a large programme using the Multi Unit Spectroscopic Explorer (MUSE) instrument at the ESO Very Large Telescope. The MUDF survey is collecting ≈150 h on-source of integral field optical spectroscopy in a 1.5×1.2 arcmin^2 region which hosts several astrophysical structures along the line of sight, including two bright $z \approx 3.2$ quasars with close separation (≈500 kpc). Following the description of the data reduction procedures, we present the analysis of the galaxy environment and gaseous properties of seven groups detected at redshifts $0.5 < z < 1.5$, spanning a large dynamic range in halo mass, $\log(M_h/M_\odot) \approx 11 - 13.5$. For four of the groups, we find associated Mg II absorbers tracing cool gas in high-resolution spectroscopy of the two quasars, including one case of correlated absorption in both sightlines at distance ≈480 kpc. The absorption strength associated with the groups is higher than what has been reported for more isolated galaxies of comparable mass and impact parameters. We do not find evidence for widespread cool gas giving rise to strong absorption within these groups. Combining these results with the distribution of neutral and ionized gas seen in emission in lower redshift groups, we conclude that gravitational interactions in the group environment strip gas from the galaxy haloes into the intragroup medium, boosting the cross-section of cool gas and leading to the high fraction of strong Mg II absorbers that we detect.

Key words: galaxies: evolution – galaxies: groups: general – galaxies: high-redshift – galaxies: haloes – quasars: absorption lines.

1 INTRODUCTION

In the last few decades, observations from ground- and space-based telescopes coupled to theoretical models have built the Lambda cold dark matter (ΛCDM) model. In this framework galaxies form within dark matter haloes that grow hierarchically (e.g. Gunn & Gott 1972; White & Rees 1978; Perlmutter et al. 1999). Several, and often competing, processes then lead to the growth, evolution, and final fate of galaxies inside these haloes, giving rise to the diverse morphology, colours, and structural properties of present-day galaxies. One of the major tasks of modern theories of galaxy

★ E-mail: matteo.fossati@durham.ac.uk

formation is thus to describe in detail the physical processes that underpin this observed evolution.

Galaxies grow both in mass and size (Muzzin et al. 2013; van der Wel et al. 2014) by acquiring gas either through cooling of a hot gas halo, or via cold gas streams fed by cosmic filaments (e.g. Kereš et al. 2005; Dekel & Birnboim 2006; van de Voort et al. 2011). The process of star formation converts the gas into stars and it is tightly related to the net balance of gas accretion and ejection (Bouché et al. 2010; Davé, Finlator & Oppenheimer 2012; Lilly et al. 2013; Sharma & Theuns 2019). Feedback processes related to stellar winds, supernova explosions, and active galactic nuclei eject gas back into the haloes surrounding galaxies: the circumgalactic medium (CGM). While some of this gas falls back on the galaxy in a fountain-like mode (Fraternali & Binney 2008), a fraction of it can leave the halo of galaxies contributing to the metal enrichment of the intergalactic medium (IGM; e.g. Dekel & Silk 1986; Schaye et al. 2003; Springel et al. 2005; Oppenheimer et al. 2010). Within this framework, it becomes crucial for an effective theory of galaxy evolution to understand how inflows and outflows interact and coexist within the CGM (e.g. Steidel et al. 2010; Tumlinson, Peeples & Werk 2017), that is the gaseous component surrounding galaxies.

At the same time, galaxies do not evolve in isolation, but are accreted on to more massive structures, comprising groups or clusters of galaxies. Indeed, it has long been known that galaxies in dense environments have different properties than those in less dense environments, both in terms of gas content and structural properties (e.g. Oemler 1974; Dressler 1980; Giovanelli & Haynes 1985; Balogh et al. 2004; Peng et al. 2010; Fossati et al. 2017). Environmental processes, triggered by the interactions between galaxies themselves with the hot medium in massive haloes and with the IGM further regulate the gas supply of galaxies (e.g. Boselli & Gavazzi 2006), leading to a different evolution compared to more isolated galaxies.

Significant progress has been made in understanding the gas–galaxy coevolution since the advent of large spectroscopic surveys of galaxies at $z \lesssim 1$ (e.g. SDSS; York et al. 2000 or GAMA; Driver et al. 2011). These galaxy surveys have been complemented by spectroscopic observations of quasars allowing for detailed studies of the CGM in absorption as a function of galaxy properties (including mass, star-formation rates), and their environment (e.g. Prochaska et al. 2011; Stocke et al. 2013; Tumlinson et al. 2013; Tejos et al. 2014; Bordoloi et al. 2014b; Finn et al. 2016; Kauffmann et al. 2017; Tumlinson et al. 2017). These studies reveal the ubiquitous presence of a multiphase, enriched, and kinematically complex CGM surrounding every galaxy (Werk et al. 2014, 2016). This picture of a multiphase CGM has been extended to $z > 1$ thanks to extensive observational campaigns with multi-object spectrographs on 8–10 m telescopes (e.g. Rubin et al. 2010; Steidel et al. 2010; Crighton et al. 2011; Rudie et al. 2012; Tummuangpak et al. 2014; Turner et al. 2014; Turner et al. 2017). Despite these advancements, however, our view of the CGM at early cosmic epochs has been mostly limited to star-forming galaxies at the bright end of the UV luminosity function, and to scales of ≈ 0.1–1 Mpc around galaxies, due to the difficulty in obtaining spectroscopy of samples of objects at small projected separations from the quasars using traditional multi-objects spectrographs.

These limitations have recently been lifted by integral field spectrographs which have been deployed at the largest observing facilities, including the Multi-Unit Spectroscopic Explorer (MUSE; Bacon et al. 2010) at the ESO Very Large Telescope, and the Keck Cosmic Web Imager (KCWI; Morrissey et al. 2018) at the Keck

Observatory. In particular, thanks to its large 1 arcmin^2 field of view, its extended wavelength coverage in the optical, and its exquisite sensitivity, MUSE has become the ideal instrument for studies of the CGM of galaxies in quasar fields (e.g. Fumagalli et al. 2016, 2017b; Schroetter et al. 2016; Bielby et al. 2017; Péroux et al. 2017; Klitsch et al. 2018; Chen et al. 2019).

Leveraging the unique features of this instrument, we have designed an observational campaign to acquire very deep MUSE observations in the field centred at $21^h:42^m:24^s$, $-44°:19^m:48^s$ (hereafter the MUSE Ultra Deep Field or MUDF). This field stands out for its rare property of hosting two bright quasars at $z \approx 3.22$ that probe the IGM and CGM of intervening galaxies with two sightlines ≈ 60 arcsec apart. Another quasar lies at the same redshift at ≈ 8 arcmin separation, making this system a quasar triplet (Francis & Hewett 1993). Upon its completion, this programme will acquire ≈ 200 h of MUSE data (corresponding to ≈ 150 h on source) in a 1.5×1.2 arcmin^2 region around the two quasars (ESO PID 1100.A$-$0528). This programme is complemented by deep high-resolution spectroscopy of the quasars using the UV and Visual Echelle Spectrograph (UVES; Dekker et al. 2000) at the VLT (ESO PIDs 65.O$-$0299, 68.A$-$0216, 69.A$-$0204, 102.A$-$0194), and by the deepest spectroscopic survey (90 orbits in a single field) in the near-infrared using the Wide Field Camera 3 instrument on board the *Hubble Space Telescope*, together with deep eight-orbit near UV imaging (*HST* PIDs 15637 and 15968).

These combined data sets will enable us to achieve several goals. First and foremost, we will connect the presence of gas in the CGM of galaxies with their properties and their environment from $z \approx 3$ to the present day. Without a pre-selection for UV and optically bright sources, we will have a unique vantage point on the low mass galaxy population up to $z \sim 3$. Furthermore, the MUDF hosts notable structures as a function of redshift. For instance, a correlated strong H I absorber detected in both sightlines at $z \approx 3$ hints at an extended structure running across the field of view (D'Odorico, Petitjean & Cristiani 2002). Moreover, the presence of a quasar pair is suggestive of an overdense region at $z \approx 3.22$, which is predicted to lie at the intersection of filaments in the cosmic web. Indeed, in the first paper of this series, Lusso et al. (2019) studied the morphology of the giant Ly α nebulae surrounding the quasars, finding an elongation of the ionized gas along the line connecting the two quasars. In the future, once we have the full data set, we will search for the presence of ionized gas in this putative filament. The depth of the observations will also provide spectra of exquisite quality for a few hundred objects. Thanks to our multiwavelength data set from the near-UV to the near-IR, we will study the properties and structure of low-mass galaxies across a large fraction of cosmic time.

In this paper, we present the survey design and the details of the MUSE observations and data reduction. As a first application we focus on the connection of enriched cool gas ($T \sim 10^4$ K), as traced by the Mg II $\lambda\lambda$ 2796, 2803 Å absorption doublet in the quasar spectra, with the galaxy population and its environment at $0.5 < z < 1.5$. Even though the full MUSE data set is still being collected, the observations available to date already provide an excellent data set for an accurate reconstruction of the local galaxy environment, and of the physical properties of galaxies at $z \lesssim 1.5$. Several studies have used the Mg II doublet to trace gas with similar column densities to that detected through 21-cm atomic hydrogen observations (e.g. Bergeron 1986; Steidel, Dickinson & Persson 1994; Chen & Tinker 2008; Kacprzak et al. 2008; Chen et al. 2010; Gauthier 2013; Bordoloi et al. 2014a; Nielsen et al. 2015; Schroetter et al. 2016; Nielsen et al. 2018; Rubin et al. 2018a,b). These studies have found that Mg II absorbers trace the CGM of galaxies and

possibly outflowing gas up to a distance of ∼100 kpc (Kacprzak et al. 2008; Chen et al. 2010). This transition is therefore ideal to study the CGM of galaxies in groups and in isolation in the MUDF, for the first time in a very deep and complete data set.

The paper is structured as follows: first we present the MUDF survey strategy, the data reduction procedures, and the quality validation of the MUSE data (Section 2), and of the high-resolution UVES spectroscopy (Section 3). We then describe the procedures adopted to extract the sources and their properties (Section 4), and the reconstruction of the local environment by searching for groups of galaxies in the field (Section 5). In Section 6, we describe a novel method to fit the high resolution quasar spectra to extract metal absorption profiles and we present our results on the correlation of absorbers and galaxies in groups and in isolation. We conclude with a discussion of these results (Section 7) and with a summary of our findings (Section 8).

Throughout this paper, we assume a flat ΛCDM cosmology with $H_0 = 67.7 \, \text{km s}^{-1} \, \text{Mpc}^{-1}$ and $\Omega_{\text{m}} = 0.307$ (Planck Collaboration XIII 2016). All magnitudes are expressed in the AB system, distances are in proper units, and we assume a Chabrier (2003) stellar initial mass function.

2 MUSE OBSERVATIONS

2.1 Survey strategy and current status

The science goals of the MUDF programme include the study of the galaxy population around and along the line of sight to the quasar pair, a deep search for Lyα emission from the putative filaments which are expected to connect the two quasars at $z \approx 3.22$. Because the projected distance of these quasars is ≈62 arcsec on the sky, a single Wide Field MUSE pointing of 60 arcsec on a side (the exact shape is trapezoidal) would not allow a full mapping of the area of interest. For these reasons, we designed an observational strategy that includes two heavily overlapping pointings: North–West and South–East (hereafter named simply North and South), the centres of which are shown as black crosses in Fig. 1. Throughout the entire survey, we plan to collect ∼200 frames dithered around each of these centres. The nominal exposure time of each frame is 1450 s and different frames include small on-sky dithers (≈3–4 arcsec), as well as 10 deg rotations of the instrument to reduce systematic errors arising from the different response of the 24 spectrographs and detectors of MUSE. While multiple exposures will be taken at the same rotation angle, the sequence of dithers has been designed to ensure that those exposures will not have the same centre and orientation.

The final survey footprint will be ellipsoidal, with a ≈−45 deg position angle (North through East), and a major and minor axis of ≈110 and 90 arcsec respectively. At the time of writing, we have reached ∼ 35 per cent completion, and Fig. 1 shows the exposure map generated with these data overlaid on a combination of white-light images from the MUSE data itself and from the Dark Energy Survey (DES) Data Release 1 (Abbott et al. 2018) outside the MUSE footprint. The survey design prioritizes the collection of deeper data in the area between the two quasars, where our science goals warrant maximum sensitivity. The outer black dashed contours mark the regions with at least 15 and 30 h of exposure, respectively.

The instrument set-up makes use of the MUSE Wide Field Mode with extended wavelength coverage in the blue (4650−9300 Å), in order to search for Lyα emitting galaxies down to $z \approx 3$. We also take advantage of the Ground Layer Adaptive Optics module (GALACSI) which uses artificial laser guide stars to improve the
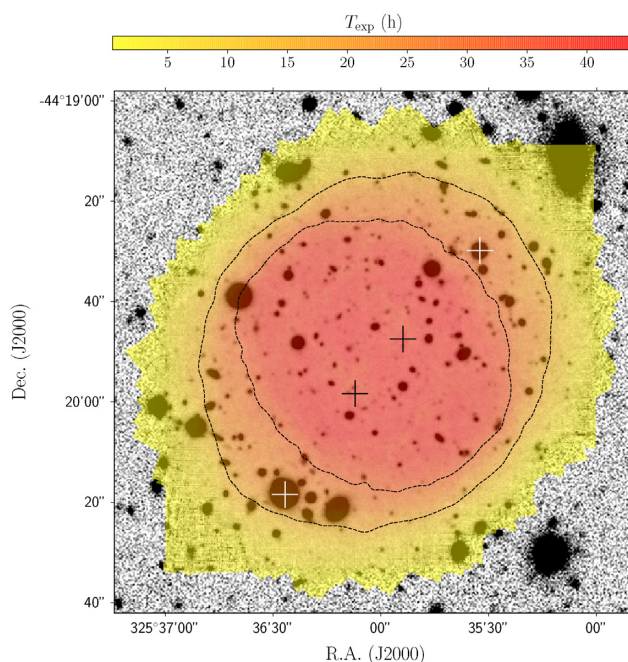

Figure 1. Exposure map (colour scale) of the MUSE observations in the MUDF overlaid on an optical white light image from the MUSE data where available or from the Dark Energy Survey combined *g*, *r*, *i* images elsewhere (shown in grey on the same surface brightness scale). North is up and East is left. The outer and inner black dashed contours mark the regions with at least 15 and 30 h of exposure, respectively, in this partial data set. The black and the white crosses mark the pointing centres and the position of the two quasars, respectively.

image quality by partially correcting for atmospheric turbulence. In this way, the observations can be performed under a wider range of natural seeing conditions without compromising the image quality of the final mosaics. However, this set-up implies that we cannot use data between 5760 and 6010 Å, a range affected by the sodium line generated by the laser beam. Moreover, laser induced Raman scattering of molecules in the atmosphere creates emission lines outside this range. These lines are removed as part of the sky subtraction data reduction steps with no impact on the data quality.

In this paper, we present results obtained with the first 44.1 h of observations. The data are collected as part of ESO programme 1100.A-0528. The first run (A) was executed in visitor mode on 2017 August 16, where we acquired 19 exposures of 1270 s each in dark-time. The conditions were excellent with clear skies and an image quality of 0.4–0.6 arcsec in the final reconstructed frames. After this successful run, further dark-time observations have been executed in service mode (runs B and C) under similarly good observing conditions. As of 2019 June, we have acquired 93 frames with an exposure time of 1450 s each. In total we have acquired 159 ks of data, corresponding to 44.1 h. The image quality on the final coadd has a full width at half-maximum, FWHM = 0.57 arcsec as measured by Moffat profile fits to point sources.

2.2 Data reduction

The data reduction procedure follows the methodology described in previous works by our team (Fumagalli et al. 2016, 2017a; Lofthouse et al. 2019). In brief, we use the ESO pipeline (v2.4.1; Weilbacher & et al. 2014) to reduce the calibrations (bias, flat, arcs, and standard stars) and apply them to the individual exposures. We

also use this software to resample the detector values into cubes that are then sky subtracted using models of the sky continuum and sky lines that are matched to the data extracted from the darkest pixels in each frame. The individual exposures are then aligned by using the position of point sources in the field, and we generate a first coadd of the frames. We register this initial coadd to match the WCS coordinates of the two quasars from the Data Release 2 of the *GAIA* survey (Gaia Collaboration 2018). The combination of relative offsets (arising from dithers) and this absolute WCS offset (arising from the pointing accuracy of MUSE) is then propagated into the pixel-tables of each exposure. We then reconstruct the cubes again for each exposure, this time on a pre-defined spatial grid of 540×540 pixels, with each voxel (volumetric pixel) measuring 0.2 arcsec in the spatial direction and 1.25 Å in the spectral direction. The size of the grid has been chosen such that all the spatially aligned exposures of the programme will fall on to it, which eliminates the need for re-projecting the data when new observations are acquired.

The cubes produced by the ESO pipeline are not yet fully science-grade, as they are still affected by an uneven spatial illumination and by residuals from sky lines subtraction (Bacon et al. 2017). To correct for these effects, we post-process the individually aligned, reconstructed, and un-skysubtracted exposures using routines from the CUBEXTRACTOR package (v1.8, CUBEX hereafter, Cantalupo in preparation; see Cantalupo et al. 2019 for a description of the algorithms). The adopted procedure follows earlier work using MUSE data (Borisova et al. 2016; Fumagalli et al. 2016, 2017a).

In brief, we use the CUBEFIX tool to correct residual differences in the relative response of the 24 MUSE IFUs and of individual slices, which are not fully corrected by flat-field calibration frames. CUBEFIX improves the illumination uniformity by measuring the average illumination in each stack (the MUSE FoV is composed of 24 IFUs which are further made of 4 stacks of 12 slices), as a function of wavelength on white-light images generated on-the-fly from the cube. We then use the CUBESHARP tool for sky subtraction. The algorithm performs a local sky subtraction, including empirical corrections of the sky line spread function. The combination of these two routines is applied twice, by using the first illumination-corrected and sky-subtracted cube to mask the sources in the field for the second iteration. The masking step is critical to measure the true instrumental illumination in each stack and to achieve a high-quality sky subtraction.

After this first double pass of the CUBEX tools on the individual frames, we coadd them with mean statistics and 3σ clipping to generate a deep white light cube. This cube is then used to detect and mask the sources and the deep mask is then fed into CUBEFIX and CUBESHARP for a final run. After this step we measure the FWHM of point sources, their average flux, and their position with respect to the *GAIA* astrometry using Moffat fits to the white light images of each exposure. The distribution of these values across all the exposures are then inspected to ensure that all the frames are correctly aligned and flux calibrated. The photometry is consistent at a 4 per cent rms level across frames and the astrometric precision is within 0.05 and 0.03 arcsec in RA and Dec. respectively, i.e. < 10 per cent of the spatial resolution. Moreover, no frame has been identified to be a $>3\sigma$ outlier on any of these metrics and therefore we include all frames in the final combine.

Lastly, we combine the individual cubes with a 3σ clipping rejection of outliers and both with mean and median statistics. We also generate mean combines obtained with two independent halves of the exposures. These products are useful to correctly identify weak emission-line sources in the cube from residual artefacts (e.g. residuals of cosmic-ray hits), which are likely to appear only in one
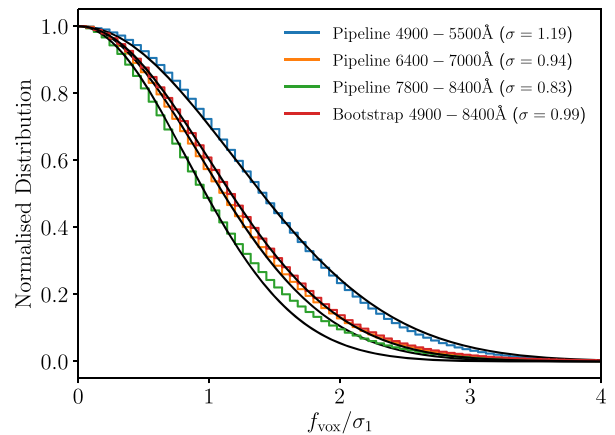
Figure 2. Histograms of flux in voxels values, normalized by the voxel standard deviation from the ESO + CUBEX pipeline in three wavelength ranges (blue, orange, and green), and in the full wavelength range after reconstructing the variance cube using a bootstrap resampling technique (red). Shown with black lines are Gaussian fits to these distributions, with the resulting standard deviation listed in the legend. Only spatial pixels free from continuum sources are included in this analysis.

of the two independent combines. The CUBEX reduction pipeline significantly improves the quality of the illumination uniformity across the entire observed area. We quantified the flatness of the illumination by comparing the standard deviation of the flux in sky pixels of the white-light image from the CUBEX processing relative to the ESO reduction, finding a ratio of 0.23. This means that the products used in this work are four times deeper than what would have been possible to achieve with the standard pipeline.

2.3 Noise characterization

During each step of the reduction process, the Poisson noise from detector counts is propagated and then combined into a cube that contains the variance of the resampled flux values. However, during several steps, including the drizzle interpolation on to the final grid, the propagated variance departs from accurately reproducing the effective standard deviation of individual voxels in the final data cube (see Lofthouse et al. 2019). In Fig. 2 we show the flux distribution of voxels ($f_{\rm vox}$) normalized by the pipeline error (σ_1) in each pixel within three wavelength intervals that are increasingly affected by atmospheric sky lines (namely 4900–5500 Å, 6400–7000 Å, and 7800–8400 Å, in blue, orange, and green, respectively). Once sources are masked, the distribution is expected to approximate a Gaussian (the black lines are Gaussian fits to the distributions), with standard deviation of unity. Instead, Fig. 2 shows that the pipeline error underestimates the true standard deviation in regions free from sky lines (blue histogram, with $\sigma = 1.19$), while it overestimates it in regions more contaminated by skylines (green histogram, with $\sigma = 0.83$). Moreover, the distribution of $f_{\rm vox}/\sigma_1$ in the wavelength interval $7800 - 8400$ Å shows the largest departure from a Gaussian distribution, an effect that could be attributed to the second-order contamination of the spectra due to our use of the MUSE extended wavelength mode.

We overcome this issue by bootstrapping the combination of individual exposures for each pixel to accurately reconstruct the noise in the final mean, median, and half-exposure cubes. For this, we use 10 000 realizations of the bootstrap procedure to produce a variance cube. We then inspect the flux distribution of pixel
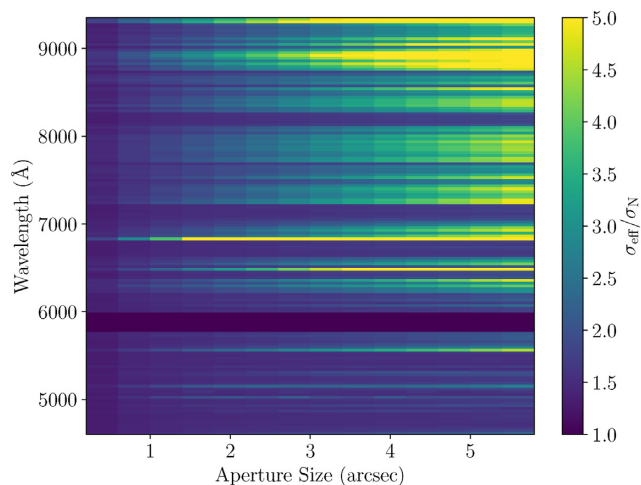
Figure 3. Ratio between the flux dispersion in apertures of varying size ($\sigma_{\rm eff}$) and the error derived propagating the variance ($\sigma_{\rm N}$), as computed across the MUDF datacube in a 5 Å window (4 pixels) as a function of wavelength and aperture size. The dark stripe just below 6000 Å is the region without valid data due to the scattered light from the AO laser.

values divided by the standard deviation of this new error, finding a distribution much closer to Gaussian, although still offset by a few per cent from unity. We attribute this offset to a non-Gaussian distribution of the $f_{\rm vox}$ values. Due to this small offset, we further rescale the bootstrap variance cube to obtain a distribution of $f_{\rm vox}/\sigma_1$ that is unity on average, as shown by the red line in Fig. 2. We also note that by adopting this improved variance cube, the trend with wavelength which affects the propagated variance is also removed.

Lastly, we derive a model for the correlated noise arising from the resampling of the pixel tables on to a final grid, as described in Lofthouse et al. (2019). This model represents the correction that needs to be applied to the propagated error for a source in a square aperture of N spatial pixels on a side, $\sigma_{\rm N}$, to recover the effective noise, $\sigma_{\rm eff}$. In the spectral direction we use an aperture of 4 pixels (≈ 5 Å) which is generally appropriate for narrow emission lines in galaxies. Fig. 3 shows this correction in bins of wavelength and aperture size. While the dependence with aperture size is a smooth and monotonic function, the wavelength trend is not trivial to understand. It does not correlate to the brightness of sky lines, and we hypothesize it might be driven by the optomechanical design of the instrument, by our observing strategy, or more likely by a combination of the two. Regardless of the physical origin, when using these data to search for line emitters, we will use a second-order polynomial fit that describes $\sigma_{\rm eff}/\sigma_{\rm N}$ as a function of the aperture size, for the wavelength bin where each source is found.

3 HIGH-RESOLUTION QUASAR SPECTROSCOPY

As part of the MUDF survey, we are collecting a set of ancillary data to complement the MUSE observations. In this work, we make use of UVES high-resolution spectroscopy of the two quasars, J214225.78-442018.3 (also known as Q2139 − 4434, and hereafter QSO-SE) at $z = 3.221 \pm 0.004$ and J214222.17-441929.8 (Q2139 − 4433, hereafter QSO-NW) at $z = 3.229 \pm 0.003$ (Lusso et al. 2019), for which we provide a description of the data acquisition and data reduction.

Some UVES data for the two quasars already exists in the ESO archive (PIDs 65.O-0299, 68.A-0216, 69.A-0204; D'Odorico et al. 2002). These data cover the wavelength range ≈4100–9000 Å, with a gap between ≈7400 and 7500 Å, due to the gap between the two CCDs in the red arm of UVES. The S/N of the bright quasar is ≈25 per pixel across most of the wavelength range, while the fainter quasar has a S/N ≈8 per pixel. To increase the wavelength coverage (down to ≈3600 Å and to fill the current gaps) and to increase the S/N of the fainter quasar, we have been awarded a total of 23 h of new UVES observations (PID 102.A−0914). At the time of writing, observations for QSO-SE have been completed for a total of 7 h on-source, while for QSO-NW only 15.5 h were obtained, and 17 h are still to be observed. In this paper, we therefore make use of the full data set for the brighter quasar, relying only on a partial data set for the fainter one. We will describe the spectra obtained from the complete observations in a forthcoming paper.

All data were reduced with the current version of the UVES pipeline (v. 5.10.4), using default parameters and procedures. At the end of the standard reduction process, the non-merged, non-rebinned spectra were reformatted with a custom script and input to the ESPRESSO Data Analysis Software (DAS; Cupani et al. 2016) for the final operations of coaddition and continuum fitting. This step avoids multiple rebinning of the spectra, which would introduce correlations in the error array. Spectra have been normalized to the continuum estimated by the ESPRESSO DAS. This software fits a cubic spline to the spectrum redwards of the Ly α emission. In the Ly α forest, the fit is iteratively improved by the simultaneous fit of the Ly α absorption lines (for more details see Cupani et al. 2016). The final continuum-normalized spectra were then rebinned to a constant velocity step of 2.5 km s^{-1}.

4 THE GALAXY POPULATION IN THE MUDF

In this section we characterize the galaxy population detected in the MUDF and describe the procedures used for the identification of continuum sources, the extraction of their spectroscopic redshifts, and the derivation of their physical properties through stellar population synthesis fits.

4.1 Source detection

We identify continuum sources using the SEXTRACTOR (Bertin & Arnouts 1996) software on the white light image reconstructed from the MUSE datacubes. We input a variance image and we use a conservative threshold of 3σ above the local noise, and a minimum area of 10 pixels for detection. The minimum deblending parameter DEBLEND_CONT is set to 0.0001, chosen to enable the detection of sources in crowded regions of the mosaic. We restrict source extraction to the area where we collected more than 10 exposures, corresponding to an observing time of ≈4 h, to avoid spurious detections at the noisy edges of the field of view. In future publications we will use deep *HST* imaging for source detection in the field.

This procedure identified 250 sources. For each of them, we extract the magnitude in the detection image ($m_{\rm MUSE}$) in an elliptical aperture with size equal to 2.5 times the Kron (1980) size from SEXTRACTOR. We also reconstruct a 1D spectrum summing the spectra from pixels within the Kron aperture, also transforming the wavelength to vacuum. In both these procedures, we mask nearby sources whose segmentation map falls in the extraction mask to minimize the effects of blending.

Table 1. The properties of the continuum sources in the MUDF extracted by SEXTRACTOR with S/N > 3. Column 1 shows the source ID, column 2 shows the source name. Columns 3 and 4 list the right ascension and declination of the sources followed by the MUSE white-light magnitude of the source in column 5 with its associated error (column 6). The redshifts obtained using MARZ are shown in column 7 followed by their confidence (column 8). A confidence flag of 3 or 4 indicates reliable redshifts while flags 1 or 2 are for unknown or highly uncertain redshifts, respectively. Column 9 shows the stellar mass from stellar population fitting for sources with $z < 1.5$. The full table is included as online only material.

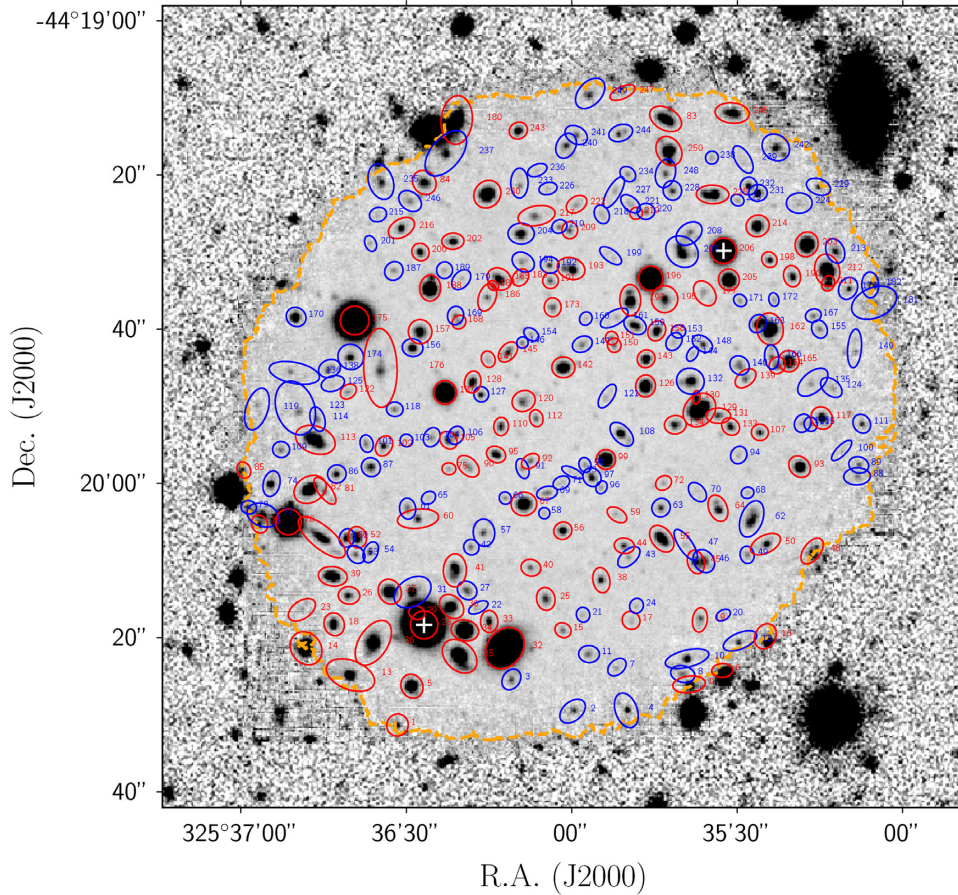| ID	Name	RA (J2000)	Dec. (J2000)	m_{MUSE}	$\sigma_{m_{MUSE}}$	Redshift	Confidence	$\log(M_*/M_\odot)$
1	MUDFJ214226.11-442031.3	325.60878	−44.34204	24.3	0.2	4.0441	4	–
2	MUDFJ214223.99-442029.5	325.59996	−44.34154	26.0	0.3	–	1	–
3	MUDFJ214224.73-442025.4	325.60304	−44.34039	25.7	0.3	–	1	–
4	MUDFJ214223.34-442029.4	325.59725	−44.34151	24.3	0.1	–	1	–
5	MUDFJ214225.93-442026.3	325.60805	−44.34064	23.6	0.1	1.0530	4	10.24

Figure 4. Reconstructed optical white-light image from the MUSE data (where available) or from the DES *g*, *r*, *i* images (outside the MUSE FoV). North is up and East is left. The two quasars are marked with white crosses. Continuum-detected sources identified within the MUSE field are marked with apertures (red for sources with spectroscopic redshifts with confidence classes 4 and 3) with size equal to six times the Kron radius. The dotted orange contour encloses the region where the exposure time is ≥4 h.

We measure redshifts using the MARZ software (Hinton et al. 2016), which we customize[1] with the inclusion of high-resolution synthetic templates for passive and star-forming galaxies at $z < 2$ derived from Bruzual & Charlot (2003) stellar population synthesis models. Following automatic template fitting, individual sources are inspected and classified by two authors (MFo and EKL) in four classes (4, secure redshift with multiple absorption or emission features; 3, good redshift with single but unambiguous feature; 2, possible redshift, based on a single feature; 1, unknown

redshift). Typical redshift uncertainties are $\delta z \approx 0.0002 \times (1 + z)$, corresponding to $\delta v \approx 60\,\mathrm{km\,s^{-1}}$.

The final redshift classification is presented in Table 1. Fig. 4 shows the position within the MUDF footprint of the continuum-detected sources and their SEXTRACTOR IDs. Hereafter we make use only of the objects with a reliable spectroscopic redshift (classes 3 and 4) which are marked with red apertures. The redshift distribution of these 117 sources (47 per cent of the detected sample) is shown in Fig. 5. The range $1.5 < z < 2.5$, known as the 'redshift desert', does not have significant detections due to the absence of strong emission lines that would fall within MUSE coverage. Only two galaxies are identified there thanks to strong Al III absorption lines in their
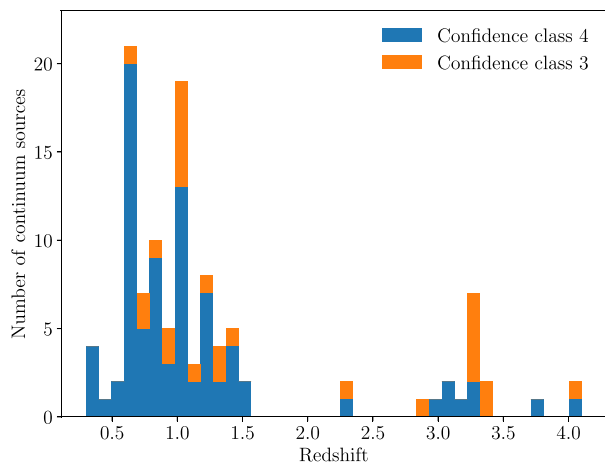
[1]This version is available at https://matteofox.github.io/Marz

Figure 5. Distribution of spectroscopic redshifts with confidence classes 4 and 3 (see the text for details) for continuum sources in the MUDF.

Figure 6. Top panel: Number of galaxies extracted as a function of the magnitude in the detection image. The grey dashed line shows the expected number of galaxies determined from a linear fit to the region between $m_{MUSE} > 24$ mag and $m_{MUSE} < 26.5$ mag. Bottom panel: Fraction of mock sources detected by SEXTRACTOR. The solid lines are for the injection of Gaussian sources with a FWHM of 0.6 arcsec. The dashed lines are for sources with an exponential profile with scale-length equal to 0.26 arcsec and PSF convolved. Lines of different colours are for different exposure times in the MUDF map. The arrows (filled for point sources and empty for extended ones) mark the faintest magnitude at which we are 90 per cent complete in each bin of exposure time. The black points (with error bars) show the empirical detection fraction determined as the ratio of the detected galaxies relative to the expected number from the linear fit in the top panel.

Table 2. Name and wavelength range of the top-hat filters defined for the photometric extraction.

Filter Name	λ_{min} (Å)	λ_{max} (Å)
MUSE Blue	4750	5700
MUSE Green	6100	7100
MUSE Red	7100	8200
MUSE NIR	8200	9300

spectra. This range, however, will be filled in by the ultra-deep near-infrared observations which we are collecting with *HST*/WFC3.

4.2 Completeness

To assess the completeness of our source extraction procedure, we inject mock sources of known magnitude into the detection (white-light) image and we assess their detection rate. First, we inject 2D Gaussian templates with a FWHM of 0.6 arcsec to simulate unresolved point sources at the resolution limit of the final MUSE mosaic. Then, we repeat the experiment using circular exponential profiles which are more appropriate for real disc-like galaxies. In this case we use an exponential scale length of 0.26 arcsec which corresponds to an effective radius of 5 kpc at $z \sim 1$, which is typical for star-forming galaxies (van der Wel et al. 2014). The intrinsic exponential profiles are convolved with a Gaussian kernel with a FWHM of 0.6 arcsec to account for the effects of the observational PSF, and do not include the effects of the disc inclination. In each iteration, we inject 80 mock sources (to avoid confusion and blending issues) in blank background regions and we repeat the detection procedure 10 000 times.

The bottom panel of Fig. 6 shows the fraction of detected mock sources as a function of magnitude for sources injected at locations of the image with different exposure times. For point sources (solid lines) we reach fainter limits than for extended sources (dashed lines), due to their compactness. The arrows mark the faintest magnitude at which we are 90 per cent complete in each bin of exposure time. In the deepest bin, where we have so far collected between 30 and 45 h of data, we reach $m_{MUSE} \simeq 27.8$ and 26.6 mag for point-like and extended sources, respectively. The top panel of Fig. 6 shows the number of detected galaxies as a function of the white-light magnitude, m_{MUSE}. We fit a linear relation (dashed line) to the logarithm of the number counts in the region 24 mag $< m_{MUSE} < 26.5$ mag, where our survey is complete. We then show in the bottom panel the empirical detection fraction (black points) determined as the ratio of the detected galaxies relative to the expected number from the linear fit. Despite the low number statistics, we find that this empirical detection fraction is in between the limits defined by the two mock experiments (point sources and extended sources), complementing and corroborating the approach based on mocks.
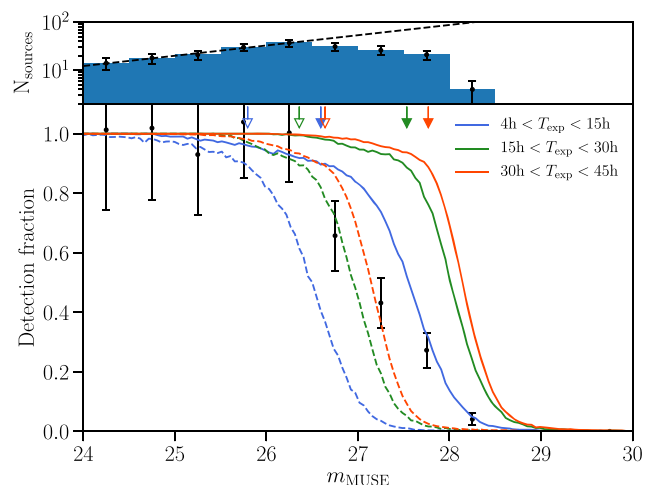
Lastly we note that, to reach maximum depth, the detection image is obtained from the full MUSE wavelength range, which does not correspond to the most commonly used broad-band filters. To facilitate the comparison to other imaging surveys we have computed the following colour corrections for a star-forming (passive) galaxy template at $z = 1$: $m_{MUSE} - r_{SDSS} = -0.31(-0.44)$, and $m_{MUSE} - i_{SDSS} = 0.04(0.05)$.

4.3 Source photometry and ancillary data

Taking advantage of the wide wavelength coverage of MUSE, we extract source photometry in four pseudo-filters with the goal of characterizing the physical properties of the galaxy population. The width and the number of filters have been carefully selected to maximize our sensitivity to strong breaks in the galaxy spectra, while keeping a good S/N ratio in the measurements, and avoiding the gap in the spectra due to the AO laser filter. We convolve the MUSE datacube with the top-hat filters, whose ranges are given in Table 2, to generate an image and the associated variance. We then run a forced photometry algorithm using apertures with radius $2.5\times$ r_{Kron} as defined above for the detection image.

The MUSE data probe the rest-frame near-UV to optical region of the galaxy spectra for sources at $z \lesssim 1.5$. While providing a good sensitivity of the recent star-formation activity and stellar content of the galaxies, these blue wavelengths are affected by dust extinction which could bias our reconstruction of the galaxy parameters.

To mitigate this issue, we include in our analysis data taken with the IRAC (Fazio et al. 2004) instrument onboard the *Spitzer* (Werner et al. 2004) Space Telescope. IRAC imaging of an area of the sky including the MUDF has been taken during the cryogenic mission (PID: GO-3699; Colbert et al. 2011) using the four channels at 3.6, 4.5, 5.8, and 8.0 μm. However, due to the field of view offset of the IRAC camera, only the channels at 3.6, and 5.8 μm cover the MUDF in its full extent, and we use them in this work. The total integration time per pixel of these observations are 1800 s, and image FWHM is ≈1.8 arcsec.

To extract IRAC photometry from these images we use the T-PHOT software (Merlin et al. 2015), which optimally deals with the lower resolution of IRAC data in crowded fields by means of source priors from higher resolution imaging. We use the MUSE white light image, PSF model, and source catalogue as the high resolution data set. We then derive a Gaussian convolution kernel for each IRAC channel, to transform the MUSE PSF into the IRAC one. Lastly we resample the IRAC data on to the MUSE pixel grid and run T-PHOT. Due to the shallowness of the IRAC data, only the relatively bright sources can be detected robustly, especially in crowded areas of the MUDF. In the end, we visually inspected the T-PHOT results for each source to assess if results: (i) can be used and the detection is at least with 3σ significance; (ii) can be used as an upper limit; (iii) cannot be used because the source is faint and it is highly blended with a nearby bright source. In the first two cases (95 per cent of the sources we fit), we include the IRAC data in the estimates of the stellar populations as described in the following section.

4.4 Stellar population parameters

We characterize the physical properties of the galaxy population in the MUDF by jointly fitting the MUSE spectra and the photometric data derived from MUSE and IRAC as described above. These combined data sets allow us to derive reliable estimates for the star-formation history, stellar mass, current star-formation rate, and dust content of the galaxies. This multiwavelength approach is instrumental in breaking the degeneracy that often arise between these parameters, most notably between stellar mass and dust extinction, or star-formation rate and galaxy age (Wuyts et al. 2011; Fossati et al. 2018). In this work, we primarily use the derived stellar masses, and we postpone the discussion of results involving the other quantities to a follow-up paper, where we will re-assess the quality of these measurements by adding into the fitting procedure the near-UV and near-IR data that will be collected with *HST* as part of programmes PID 15637 and 15968.

To infer the source properties, we fit the observed data to synthetic models using the Monte Carlo Spectro-Photometric Fitter (MC-SPF). A more complete description of the code is given in Fossati et al. (2018); here we briefly describe the procedure and the model set. First, we build a grid of synthetic stellar spectra from the Bruzual & Charlot (2003) high-resolution models at solar metallicity. Following similar work that studied the properties of galaxies in deep fields (Wuyts et al. 2011; Momcheva et al. 2016), we use exponentially declining star-formation histories with *e*-folding times varying between 300 Myr and 15 Gyr, and galaxy ages varying between 50 Myr and the age of the Universe at the redshift of each galaxy. With the imposed minimum *e*-folding time, Wuyts

et al. (2011) found that the SFR derived with this spectral energy distribution technique matches the one obtained from UV + far-IR photometry for systems with low-to-intermediate star-formation rates (SFR $\lesssim 100\,M_\odot\,yr^{-1}$), which are likely to dominate the sources in our small field.

We further add nebular emission lines to the stellar template, by using line ratios from Byler et al. (2018) scaled to the line luminosity using the number of Lyman continuum photons from the stellar spectra. The SFH and nebular emission grids are interpolated on-the-fly during the likelihood sampling. We assume a double Calzetti et al. (2000) attenuation law to include the effects of dust attenuation. Stars older than 10 Myr and emission lines arising from them are attenuated by a free parameter, A_{old}, while younger stars are attenuated by $A_{young} = 2.27 \times A_{old}$ to include the extra extinction occurring within the star forming regions.

We jointly fit the photometric data points and the MUSE spectra at their native resolution. A third degree multiplicative polynomial is used to normalize the spectra to the photometric data and to remove large-scale shape differences between the models and the spectra, especially at the edges of the wavelength range where the MUSE response function is more uncertain. The multidimensional likelihood space is sampled by using PYMULTINEST (Buchner et al. 2014), a python wrapper for the MULTINEST code (Feroz & Hobson 2008; Feroz et al. 2013). Fig. 7 shows an example of the results obtained with this fitting procedure for a galaxy in the MUDF. With the current wavelength coverage, some degeneracy remains between dust extinction and star-formation rate. Rest-UV data from *HST* will break this degeneracy, however, in this work we primarily make use of the stellar mass estimates from the fits which are found to be well converged and free from degeneracies with other parameters.

5 GROUP IDENTIFICATION

The detection of a large number of sources with accurate spectroscopic redshifts in narrow redshift bins (see Fig. 5) is highly suggestive of the presence of overdense structures in the MUDF footprint. Indeed, overdensities spanning from compact groups to clusters and superclusters of galaxies have been detected in all the fields which have been targeted by deep and extensive spectroscopic campaigns (e.g. Scoville et al. 2007; Yang et al. 2007; Kovač et al. 2010; Diener et al. 2013; Balogh et al. 2014; Fossati et al. 2017; Galametz et al. 2018). We therefore proceed to systematically identify galaxy groups in the MUDF.

There is a rich collection of literature on finding groups in spectroscopic redshift surveys, with most methods based on a Friends-of-Friends approach (Huchra & Geller 1982; Berlind et al. 2006; Knobel et al. 2009, 2012; Diener et al. 2013). These methods link galaxies into structures by finding all objects connected within linking lengths Δr (a physical distance) and Δv in redshift space. The choice of these parameters is driven by the need to balance the competing requirements of identifying all group members without overmerging different groups, avoiding interlopers, and taking into account redshift uncertainties. In this work we search for galaxy groups at $0.5 < z < 1.5$, where the lower limit is dictated by the small volume probed at lower redshift and the upper limit is given by the redshift desert. In this range, we have highly accurate spectroscopic redshifts for all the galaxies that we aim to connect into structures. We use $\Delta r = 400\,kpc$ and $\Delta v = 400\,km\,s^{-1}$, following Knobel et al. (2009) in the same redshift range. Similar to previous works, we define a galaxy group to be an association of three or more galaxies (Knobel et al. 2012; Diener et al. 2013), independently of stellar mass or observed magnitude.
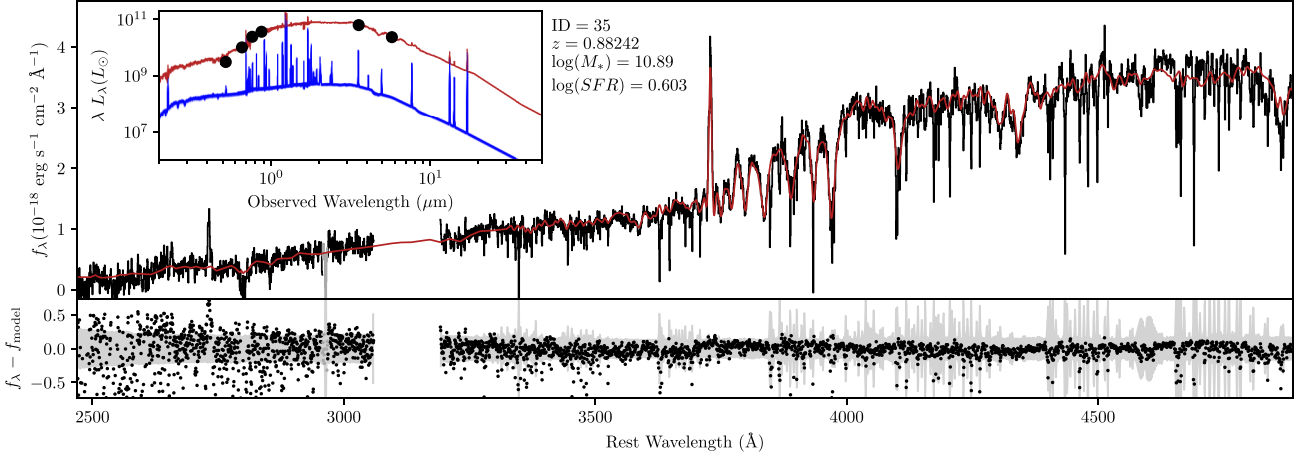
Figure 7. Example of the stellar population fitting results for source ID 35 in the MUDF. Rest-frame MUSE spectrum (black line) and best fit model (red line). The fit residuals (Data–Model) are given below the main panel, and the shaded area shows the noise array. The inset shows the spectral energy distributions extracted from the MC-SPF posterior (red lines) with the observed photometry overplotted in black. The blue lines show the contribution of young stars (Age <10 Myr) to the total template.

Table 3. Properties of the groups identified in the MUDF. The table lists: the group ID; the average RA, Dec., and redshift of the group members; the number of members in each group; the halo mass derived from the stellar-to-halo mass relation of Moster et al. (2010); the virial radius (R200) for that halo mass; the equivalent width of the Mg II λ2796 Å absorption line associated with the group (or 2σ upper limit) along the QSO-SE and QSO-NW sightlines.

ID	<RA> J2000	<Dec.> J2000	<z>	N$_{gal}$	$\log(M_{halo}/M_\odot)$	r_{vir} kpc	W_{2796} (QSO-SE) Å	W_{2796} (QSO-NW) Å
1	325.602433	−44.332283	0.67837	11	12.0	160	$0.85^{+0.03}_{-0.04}$	<0.08
2	325.598267	−44.332865	0.68531	5	11.2	87	<0.02	<0.07
3	325.593548	−44.330041	0.78491	3	10.8	61	<0.02	<0.06
4	325.597824	−44.330187	0.88205	6	12.9	293	$1.34^{+0.02}_{-0.01}$	$0.43^{+0.01}_{-0.01}$
5	325.604431	−44.331396	1.05259	15	13.4	419	$1.67^{+0.02}_{-0.02}$	<0.06
6	325.605063	−44.331111	1.15524	3	12.1	138	$1.16^{+0.06}_{-0.13}$	<0.06
7	325.602279	−44.328677	1.22849	4	11.6	96	<0.02	<0.06

Following this procedure, we find seven groups in the MUDF footprint, and their properties are listed in Table 3. We estimate the group halo mass by summing the stellar mass of the group galaxies (see Yang et al. 2007, for a validation of the method) and using the stellar to halo mass relation from Moster et al. (2010) at the redshift of the group. We also report in the table the geometric centre of the group, the average redshift of its members (not weighted by other galaxy parameters), and the virial radius calculated from the halo mass. Assuming a typical uncertainty on the total stellar mass of 0.15 dex (Conroy, Gunn & White 2009; Gallazzi & Bell 2009; Mendel et al. 2014), this turns into an error on the virial mass of 0.20–0.25 dex depending on the local gradient of the stellar-to halo-mass relation. This uncertainty corresponds to an error of ~50−60 kpc on the virial radius. The virial radius is further affected by the implicit assumption of virialization of the group halo. With only a few members per group, this cannot be guaranteed as we might be observing groups in formation. Given these caveats, the estimated virial radii should only be taken as indicative values, especially for structures with less than 10 members.

At the redshift of the groups, we search for strong line emitters which are too faint in continuum to be detected. We run CUBEX on the continuum-subtracted cube and we use the detection parameters defined in Lofthouse et al. (2019), i.e. voxel S/N > 3, minimum number of voxels of 27 and minimum number of channels in wavelength of 3. We found no line emitter that is not associated with a detected continuum source. However it remains possible that deeper exposures would lead to a secure detection of more redshifts from continuum features, possibly increasing the number of groups or including fainter members. Fig. 8 shows the location of the detected galaxies in groups within the MUDF footprint.

5.1 Going beyond the survey edges

The unprecedented depth of the MUSE observations in the MUDF comes at the price of a relatively small survey area. Therefore, it is possible that at least some of the groups identified in the previous section are part of a larger scale structure, or that some of the group members are missed by our footprint. Unfortunately, this area of the sky is not covered by wide-area archival spectroscopy, thus we can only attempt to characterize the large-scale environment around the MUDF with photometric redshifts (photo-z).

For this purpose, we downloaded source and magnitude catalogues from the DES DR1 (Abbott et al. 2018), and we computed photo-zs from the g, r, i, z fluxes using the EAZY code (Brammer, van Dokkum & Coppi 2008). Following Hoyle et al. (2018) we do not include Y-band magnitudes, because the observations are too shallow to improve the photo-z estimate. These authors also studied the photo-z uncertainty on a smaller region of the DES footprint, finding that they range from $\sigma_z = 0.1$ at $z = 0.5$ to $\sigma_z = 0.4$ at $z = 1.5$. For each group identified in the MUDF, we compute the galaxy
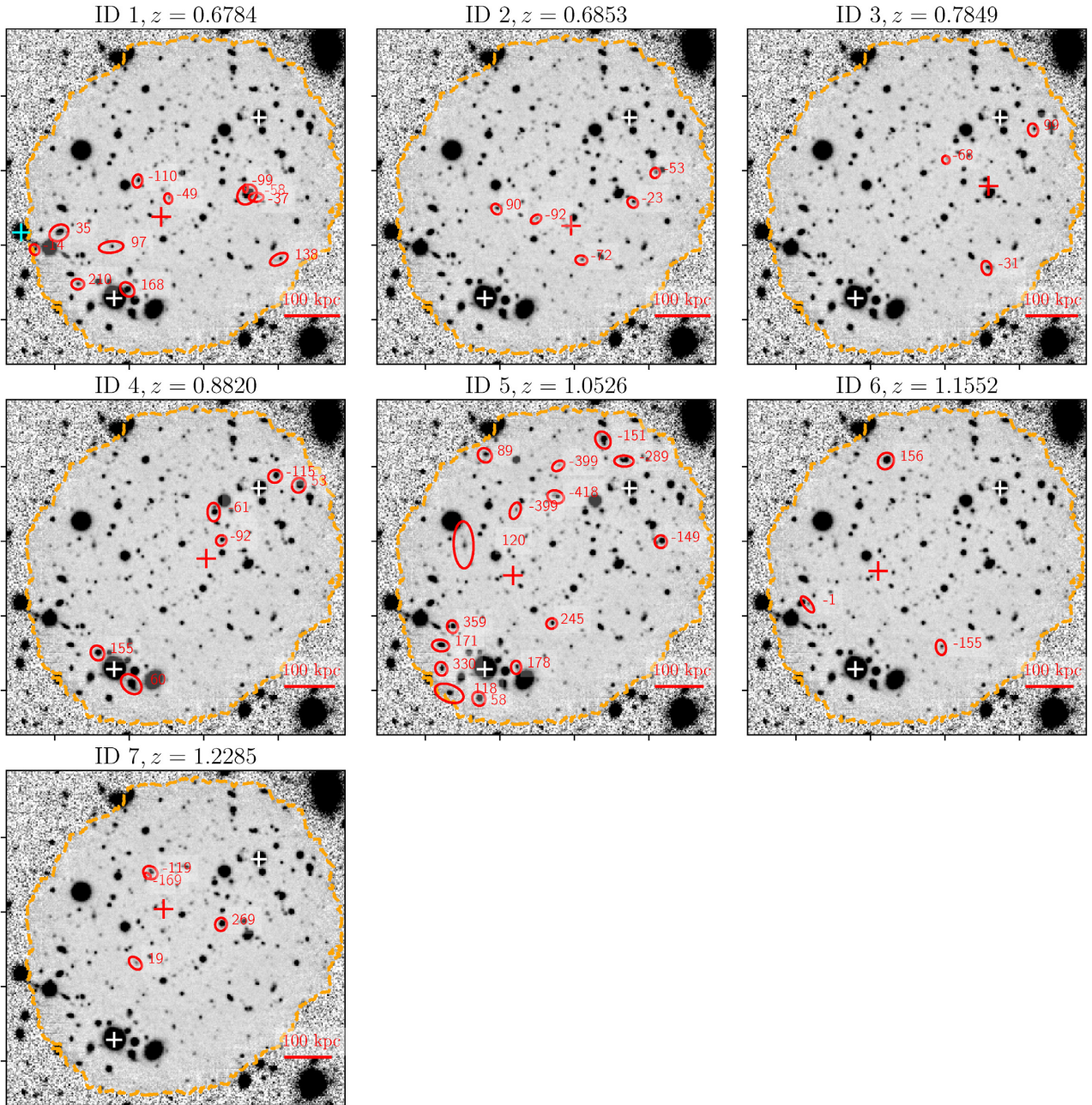
Figure 8. Gallery of the location within the MUDF of the galaxies in groups, marked with ellipses as in Fig. 4. The white crosses mark the position of the background quasars, while the red crosses in each panel indicate the geometrical centre of the group. The cyan cross in the top left-hand panel marks the position of a serendipitously detected quasar that shows absorption at the redshift of this group (see Section 6.2). The number next to each galaxy shows the velocity offset with respect to the redshift of the group. The red segment in the bottom right-hand corner of each panel marks a 100 kpc scale at the redshift of each group.

density in an aperture with radius 1 Mpc centred on the geometrical centre of the group. The density is defined as the sum over all the galaxies within this aperture of the fraction of the DES photo-z probability density function that falls within $\Delta v = \pm 5000 \mathrm{km\,s^{-1}}$ of the redshift of the group. This approach optimally takes into account the variable photo-z accuracy as a function of redshift and galaxy magnitude (Kovač et al. 2010; Cucciati et al. 2014). We then define two control apertures of the same size and velocity depth bracketing in redshift of the previous aperture, but not overlapping with it.

Despite the limitations of this approach, we do not find a significant overdensity of bright galaxies over a scale larger than the

MUDF footprint for any of the groups studied. We therefore conclude that our inferred group properties are broadly representative of the underlying population. Nevertheless, wider area multi-object spectroscopic observations are required to investigate with better precision the large-scale environment of the MUDF.

6 THE CGM OF GROUP GALAXIES

Having completed a deep census of galaxy groups including members that are as faint as $m_{\mathrm{MUSE}} \approx 28.5$ mag (or stellar masses down to $\approx 10^{8}\,\mathrm{M_*}$ at $z = 1.5$), we now take advantage of the presence of the

two bright quasars in the field to probe the gas content of galaxies within these structures in absorption. In particular, we focus on the Mg II absorbers detected in the quasar spectra at $z < 1.5$.

6.1 Mg II fitting in the high-resolution quasar spectra

To identify and fit the Mg II absorbers in the quasar spectra we employed a two step procedure. First, strong absorption lines were searched for by visually inspecting the spectra across the entire wavelength range, looking first for the Mg II doublets and then for other transitions which are commonly detected in quasar spectra, e.g. Mg I, Fe II, Mn II, Cr II, and Ca II. This procedure has been repeated by two authors independently (MFo, VDO) and for both quasars. We reliably identified five absorbers in the bright quasar at $z \approx 0.67, 0.88, 0.98, 1.05, 1.15$, while in the fainter quasar we only identify one absorber at $z \sim 0.88$.

For each identified absorber we then fit the Mg II doublet profile with a novel method that uses Bayesian statistics to identify the minimum number of Voigt components required to model the data. Our method has two desirable properties: first, it requires minimal input from the user as no initial guesses are required; secondly, the final result is an optimal statistical description of the data, as the fit does not depend on any particular choice of initial guesses nor on a user-defined prior on the number of components. The details of the algorithm used will be presented in a forthcoming publication, and are only briefly summarized here.

Once the atomic transition (or transitions in case of multiplets to be fit jointly) has been identified, it is only required to specify the wavelength range (or disjoint ranges) to fit the normalized spectrum. The code then performs a fit of the data with progressively higher number of Voigt components (between a minimum and a maximum number), where each component is defined by a column density (N), a Doppler parameter (b), and a redshift (z). For our fitting of Mg II absorbers we define uniform priors on the first two quantities in the range $11.5 < \log(N/cm^2) < 16.0$ and $1 < b/km\,s^{-1} < 30$, chosen to avoid modelling features within the noise or large-scale variations in the continuum level. The prior range on redshift is instead internally defined such that the absorption components can cover the selected wavelength range. A constant continuum level is also left as a free parameter in the fit to account for slight imperfections in the normalization of the spectra. If required following a visual assessment of the doublet profiles, we allow for a user defined number of 'filler' Voigt profiles designed to describe absorption lines arising from blends of different ions at different redshifts. One example is the rightmost line in the profile of the $z \approx 0.98$ absorber in Fig. 9. The model spectrum is then convolved to match the line spread function of the observed data using a Gaussian kernel.

At each iteration, having defined a model with n components, we sample the multidimensional likelihood space using POLYCHORD (Handley, Hobson & Lasenby 2015), a nested sampling algorithm that has better performance than MULTINEST for high-dimensional parameter spaces with multiple degeneracies between parameters. This is indeed our case, where complex models can reach a number of free parameters in excess of 50. After the sampling, we use the posterior samples to derive the Akaike Information Criterion (AIC; Akaike 1974) of each fit, defined as AIC $= 2 \times n_{par} - 2 \times \ln(L)$, where n_{par} is the number of free parameters and L is the likelihood of the model. We select as optimal fits those with a likelihood ratio within 1:150 compared to the best (lowest) AIC. If the selection includes only one model this is used as our best fit, otherwise we choose (from the selected ones) the model with the minimum number of components.

Fig. 9 shows the fits of the Mg II absorption systems identified in the quasar spectra. While the fits are jointly obtained from the 2796 and 2803 Å transitions, we show only the stronger 2796 Å transition in this figure. The single absorber found in the fainter quasar, which we discuss in more detail in Section 6.3, is shown in the Bottom Right panel, while in the other panels we show the absorbers found in the bright quasar sightline. In all panels we find complex kinematic profiles requiring from 3 to 15 Voigt components. Moreover we note that, with the exception of only one system ($z \sim 0.98$), the absorbers are found at the redshift of a galaxy group identified in the previous section. Therefore, we set the zero of the velocity axis at the redshift of the galaxy group, except for one absorber where it is set to the redshift of the closest galaxy (ID 14) in velocity space. We stress that the position of the zero on the velocity axes is only made for reference and it does not affect our results.

6.2 Connecting the absorption features and the galaxy population

The fact that Mg II absorbers are preferentially found at the redshift of a galaxy group (5/6 cases) suggests a direct connection between overdensities of galaxies and large cross sections of cold gas. Leveraging the deep spectroscopic survey in the MUDF that is complete to faint levels/low masses, we systematically explore this connection, in order to understand the physical origin of the gas probed in absorption.

We show in Fig. 9 the spectroscopic redshift of the galaxies in the MUDF which are within the plotted range for each absorber (blue stars). We immediately note two features: first, each absorber (with the exception of the one at $z \approx 0.98$) has one or more galaxies which are overlapping in velocity space with the absorption profile. Secondly, the absorbers with more complex kinematics ($z \sim 0.88$, and $z \sim 1.05$) have the largest number of galaxies at a small velocity offset. The case of the $z \sim 0.98$ absorber, instead, stands out for having a complex profile, yet a single galaxy which is offset in velocity. However, given that the bright quasar is close to the South–East edge of the observed field, we cannot rule out the presence of other objects, just outside the MUDF footprint but at smaller velocity separation compared to the galaxy we found. Another issue is that the detection of continuum sources is more difficult at small projected separation from the quasars due to their brightness. We can detect sources as faint as $m_{MUSE} \simeq 27$ mag at ≈ 25 and ≈ 18 kpc in projection from QSO-SE and QSO-NW, respectively. However, brighter or highly star forming galaxies would be detected even at smaller projected distances.

Thanks to the integral-field spectroscopic coverage of the MUDF, we next investigate trends in the spatial location of the galaxies which are found in the velocity window defined by the absorbers. Starting with the $z \sim 0.67$ absorber as a first example, we note how the Mg II profile spans a velocity range $\Delta v \sim 100-200$ km s^{-1} with respect to the redshift of the group. We recall that the latter quantity is the average of the redshift of the group galaxies, and so we should expect a roughly equal number of them above and below the average value. However, not all of them need to be distributed isotropically with respect to the quasars. In fact, by looking at Fig. 8, we find that the four galaxies with velocities overlapping with the Mg II absorber are typically closer to the bright quasar than the remaining galaxies in the group. Indeed, their average projected distance from QSO-SE is ≈ 130 kpc, while for the other galaxies it is twice as large, at ≈ 250 kpc.

Despite the large uncertainties driven by small number statistics, a similar trend emerges from the analysis of the other absorbers
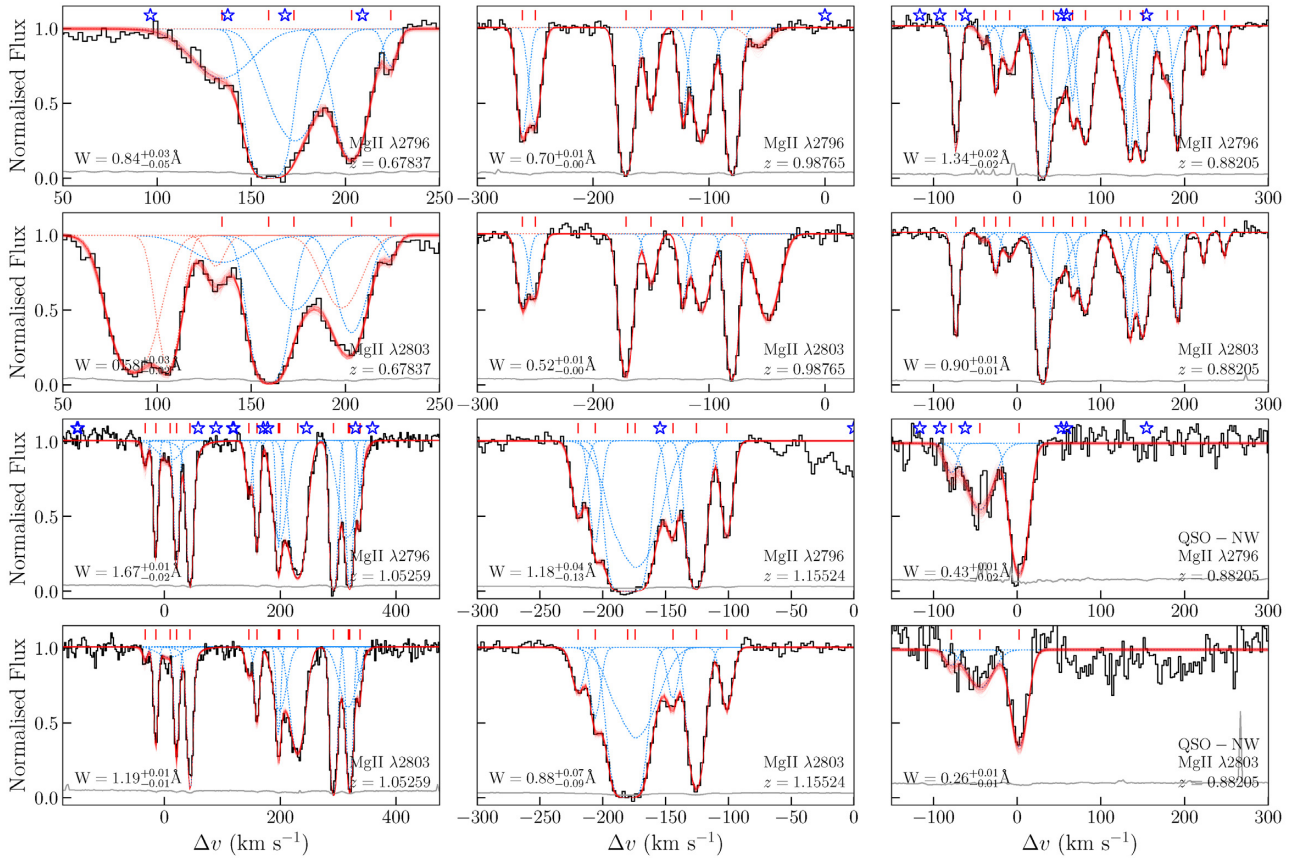
Figure 9. UVES spectra of Mg II absorbers identified in the brighter QSO-SE (all panels except last two rows in the rightmost column), and in the fainter QSO-NW (last two rows in the rightmost column). The zero velocity corresponds to the average redshift of the galaxy group associated with the absorber, or to the redshift of the closest galaxy for the $z \approx 0.98$ absorber. The observed spectrum is shown as a black histogram with the 1σ error array in grey. A Voigt profile Bayesian fitting gives the red models, where individual lines are sampled from the posterior distribution. We include the rest-frame total equivalent width measurements in each panel. The red ticks above the continuum level show the position of individual Mg II absorption components, which are shown as cyan dotted lines. The pink dotted lines are for filler components arising from blends of different transitions. The blue stars show the spectroscopic redshift of MUDF galaxies.

Table 4. Average projected distance of the galaxies which reside in groups at the same redshift of a Mg II absorber, for galaxies within the velocity window defined by the absorption profile, and outside it. For groups without an Mg II detection the average projected distance of all galaxies is given in the last column. Values without errors have only one object that satisfies the selection threshold.

z_{abs}	Group ID	$d_{in, win}$ (kpc)	$d_{out, win}$ (kpc)
0.67	1	130 ± 56	251 ± 25
0.68	2	–	257 ± 94
0.78	3	–	363 ± 92
0.88	4	274 ± 87	522
1.05	5	162 ± 41	467 ± 29
1.15	6	195	321 ± 101
1.22	7	–	322 ± 83

associated with the groups, as summarized in Table 4. This table reports the typical distance from the sightline QSO-SE of galaxies that overlap in velocity with the absorption profile ($d_{in, win}$), compared to the distance for the remaining galaxies in the group. In all cases, galaxies overlapping in velocity with the absorption profile lie at closer projected separation (by a factor of $\approx 1.5-2$) than galaxies that are not overlapping with the Mg II absorbers.

Considering instead the groups with no Mg II association (ID 2, 3, and 7), Fig. 8 reveals a lack of galaxies in the immediate surroundings of the QSO-SE line of sight, in line with the trend above. These results therefore suggest that the cold gas absorbers traced by Mg II arise preferentially from the CGM of one or multiple galaxies which are closer than ≈ 100 kpc from the quasar line of sight. It should however be noted that the probability of group galaxies giving rise to Mg II is unlikely to be exclusively modulated by proximity to the line of sight, with covering factors playing a role. Indeed, Fig. 8 shows also the presence of galaxies in close proximity to the QSO-NW line of sight (mostly from groups 3, 4, and 5) that do not necessarily give rise to absorption (see below).

The relation between the strength of Mg II absorbers and the galaxy distance has been studied extensively in the literature. For instance, Chen et al. (2010) report a large statistical sample of galaxy–quasar pairs, finding a strong anticorrelation between the equivalent width of the absorption profile and the distance of the closest galaxy. We can therefore compare directly in this parameter space the properties of MUDF galaxies, both within groups and in isolation, with the results present in the literature.

In Fig. 10, we show the rest-frame equivalent width (W) for the Mg II $\lambda2796$ Å absorption line, obtained integrating the best-fitting models derived above, as a function of the projected distance of
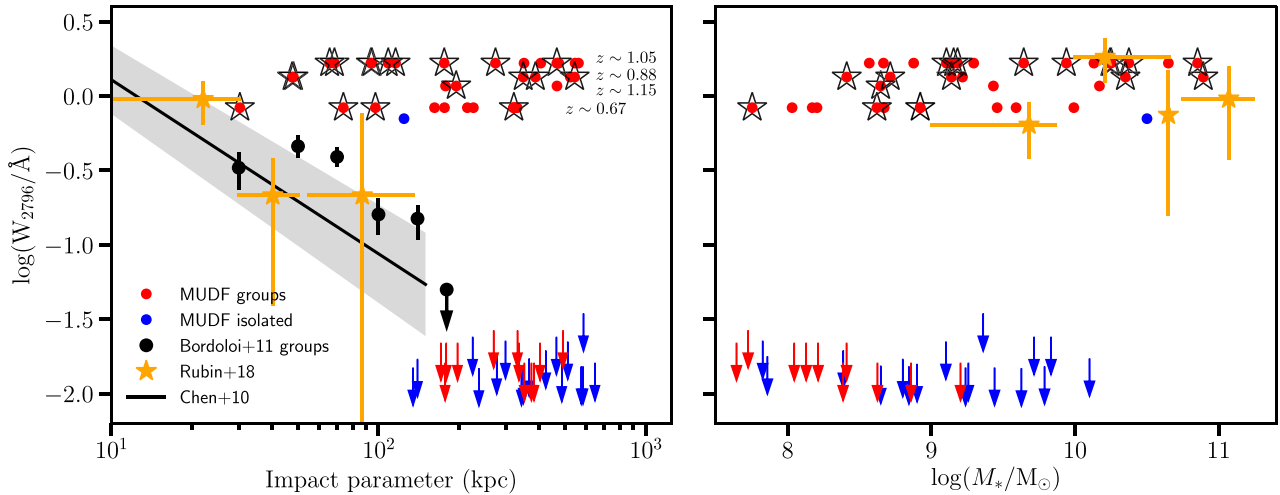
Figure 10. Rest-frame equivalent width (*W*) for the Mg II λ2796 Å absorption line as a function of impact parameter (projected distance of each galaxy from the QSO-SE sightline for MUDF galaxies, left-hand panel) and of the galaxy stellar mass (right-hand panel). Galaxies in the MUDF footprint are shown as red circles if they reside in a group and as blue circles if they are isolated. The arrows (red for galaxies in groups and blue for isolated galaxies) show 2σ upper limits measured on the UVES spectrum in a $10\,\mathrm{km\,s^{-1}}$ velocity window centred at the redshift of each galaxy. The black empty stars show galaxies which have a redshift within the Mg II absorption profile for the strong absorbers shown in Fig. 9. The redshift of the groups are shown in the left-hand panel at the y-axis levels of the corresponding values of *W*. The black line is the best-fitting relation (with the 1σ confidence area shaded in grey) between *W* and impact parameter from Chen et al. (2010). The orange stars and black circles are obtained from stacking galaxy–galaxy pairs from the sample of isolated galaxies of Rubin et al. (2018a) and the sample of group galaxies of Bordoloi et al. (2011).

each galaxy from the QSO-SE sightline (left-hand panel) and of its stellar mass (right-hand panel). Galaxies belonging to a group that is associated with an Mg II absorber are shown as red circles and they have been assigned the total *W* of the absorption profile, while the galaxy which we associate with the $z \sim 0.98$ absorption system is shown as a blue circle. For the other sources, we plot 2σ upper limits measured on the UVES spectrum in a $10\,\mathrm{km\,s^{-1}}$ velocity window centred at the redshift of the galaxy.

From this analysis, it appears that the four out of seven groups that are associated with an absorber have high equivalent width and, as noted above, have at least one galaxy which is within 150 kpc of the quasar line of sight. Moreover, these groups tend to host galaxies that are relatively massive ($\log(M_*/\mathrm{M_\odot}) > 10$) and therefore, given their CGM is likely to scale with their size (e.g. Chen et al. 2010), they are more likely to have a larger cross-section of Mg II that can give rise to the absorption.

An apparent exception is the $z \approx 0.67$ group, which seems to lack particularly massive galaxies. However, we argue that in this case the Mg II absorption is mostly driven by the fact that one galaxy, despite being of a lower stellar mass ($\log(M_*/\mathrm{M_\odot}) = 8.92$), is very close in projection (29 kpc) and its redshift places it at the centre of the absorption profile. On the other hand, for the three groups without a detection, their galaxies are both further away from the absorber and their stellar masses are low $\log(M_*/\mathrm{M_\odot}) \sim 9$, overall reducing the chances that the CGM of group members intercepts the line of sight.

This picture is further reinforced when we make the same analysis for the QSO-NW. We find that the galaxies in groups are on average further away from this line of sight compared to that of the brighter quasar. Only three galaxies are within 100 kpc, two of which are in the $z \approx 0.88$ group which we associate with the only Mg II detection in this sightline (see Section 6.3). Moreover, a third lower redshift quasar ($z \approx 1.285$; cyan cross in Fig. 8), lying close to the edge of the FoV (where no sources have been extracted) is in close spatial proximity to the $z \approx 0.67$ group. It does in fact exhibit strong Mg II

absorption at this redshift as seen from the MUSE spectrum, but we did not find other absorbers associated with groups or individual galaxies at larger separations from this third sightline. We therefore conclude that a combination of proximity to the quasar line of sight and presence of massive galaxies hosting large cross sections of cool gas are the main factors that control the high incidence of Mg II absorbers in these groups.

Having established what drives the incidence of Mg II in these groups, we now compare the absorption properties to samples of galaxies from the literature. To this end, in Fig. 10, we show the results of the analysis by Chen et al. (2010) (black solid line) and the average properties of the CGM of galaxies at $0.35 < z < 0.8$ from foreground and background galaxy pairs in the PRIMUS survey (Rubin et al. 2018a). These galaxies are not explicitly selected to be within groups. These authors find that the strength of Mg II absorption declines as a function of impact parameter (*d*, i.e. the projected separation of a galaxy from the probing sightline), with the average gas content of star forming galaxies versus *d* in the PRIMUS survey being consistent with the fitting function of Chen et al. (2010), albeit with a large intrinsic scatter for individual galaxies.

However, the total equivalent width of Mg II in galaxies within the MUDF groups is higher than the 1σ scatter of the data from Rubin et al. (2018a) when shown as a function of *d*, but are consistent with these data as a function of stellar mass. Likewise, compared to the scaling relation of Chen et al. (2010), the MUDF group galaxies lie consistently above the relation at fixed impact parameter. These results imply that the group environment has an effect on the cross-section of Mg II, leading to enhanced equivalent widths at larger distances compared to galaxies not explicitly selected within groups. Bordoloi et al. (2011) presented the radial Mg II absorption profile from a sample of group galaxies from the zCOSMOS survey finding that groups have more extended absorption profiles compared to a sample of isolated galaxies from the same survey. However, the radial profile for group galaxies is largely consistent with the one from the Chen et al. (2010) and Rubin et al. (2018a) samples. This

could be an intrinsic feature of the sample or an effect of contamination from more isolated galaxies in the group sample. Nielsen et al. (2018) studied the Mg II absorption in a sample of 29 group-like environments (defined to have at least two galaxies within 200 kpc of a background quasar and with $\Delta v < 500 \, \mathrm{km \, s^{-1}}$). These authors found that the Mg II median equivalent width in this sample is $W = 0.65 \, \text{Å}$, and it is indeed enhanced by a factor 2.2 compared to an isolated galaxy sample. This is also in line with the result of Gauthier (2013), who reported on the Mg II equivalent width for three galaxy groups associated with ultrastrong Mg II absorbers ($W > 3.5 \, \text{Å}$), which are atypical of the general galaxy population.

Finally, we comment on the properties of the only absorber associated with an isolated galaxy. The complete isolation of this source (ID 14) is unlikely, given its stellar mass ($\log(M_*/M_\odot) = 10.51$). It is possibly living in a massive halo which in turn is expected to host satellite galaxies (see below). And while this source is the closest to the quasar line of sight among individual galaxies in the MUDF, its equivalent width is still elevated for its impact parameter. Moreover, the several narrow kinematic components found in the absorption spectrum seem to suggest, in analogy with the other Mg II arising from groups, that this absorber could be associated with a group that we do not fully cover in the MUSE footprint.

6.3 Detection of cold gas absorption in the quasar pair

Up to this point, our analysis reveals that groups hosting Mg II absorbers show galaxies in closer proximity to the line of sight and host more massive galaxies, two factors that are likely to boost the incidence of Mg II absorption. Moreover, the equivalent width of Mg II appears to be elevated compared to samples not explicitly selected in groups. We now fully exploit the ability to conduct tomography in the MUDF to assess whether the observed absorbers can be attributed to a widespread intragroup medium, or whether they are more likely to be associated with individual galaxies.

The groups at $z \approx 0.88$ and $z \approx 1.05$ appear to be most suited for this analysis as they both contain a significant number of members that appear to be distributed across the two quasar sightlines. For the $z \approx 1.05$ absorber, despite a strong ($W = 1.67 \, \text{Å}$) and complex kinematic profile seen against the QSO-SE, we derive only a 2σ upper limit of $0.06 \, \text{Å}$ against the QSO-NW. For the group at $z \approx 0.88$, instead, we detect also Mg II absorption in the UVES spectrum of the fainter QSO-NW. At this redshift, we find a Mg II absorber also in the spectrum of the bright QSO-SE, which enables us to study whether the kinematics of the absorption is correlated over a scale of $500 \, \text{kpc}$. The right-hand panels in Fig. 9 show the data and Voigt profile models of the absorption systems found at $z \approx 0.88$ in both sightlines (top panel for the bright quasar and bottom panel for the fainter one). Along the line of sight of the faint quasar we find only three Voigt components, as opposed to 15 in the other sightline. These components span a much smaller velocity range ($\sim 100 \, \mathrm{km \, s^{-1}}$) compared to the absorption system found in the brighter quasar ($\sim 350 \, \mathrm{km \, s^{-1}}$). Furthermore, we do not find a significant correlation between the kinematics of the components in the two sightlines. A marginal amount of correlation could be present in the first and last (in velocity space) components seen in the QSO-NW sightline, where a component exists at a similar velocity also in the other sightline, however with a significantly different strength. This result suggests that the cold absorbing gas is not necessarily related to coherent structures in the group as a whole, which is also corroborated by the non-detection of correlated Mg II in the $z \approx 1.05$ group.
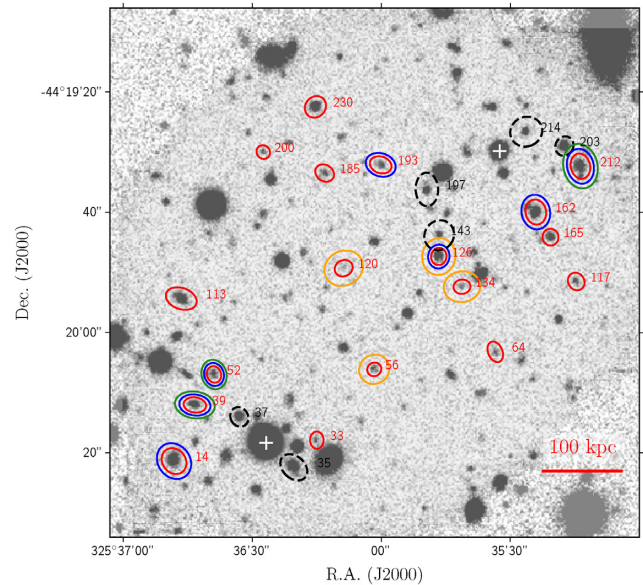
Figure 11. Location within the MUDF of the background galaxies (red solid ellipses) that we include in the spectral stack A used to search for extended Mg II absorption around the galaxies (black dashed ellipses) in the $z \sim 0.88$ group. Three more stacks (B, C, and D) include the galaxies marked with blue, green, and orange ellipses, respectively.

The lack of evidence in support of a dense and homogeneous intragroup medium leaves open the hypothesis that the enhanced absorption in the groups arises from the CGM of individual galaxies, which has been processed by the environment. Indeed, considering again the $z \approx 0.88$ group, we find near the QSO-NW line of sight a clustering of galaxies with negative velocities compared to the group average redshift, which broadly corresponds to the velocities of the absorption components in this sightline. More specifically, from Fig. 8, it appears that the galaxies lie in two sub-groups that are mostly aligned along the SE-NW direction. The fact that both quasar sightlines go through the direction of this alignment is a possible explanation for why this group is the only one detected in both sightlines.

Thanks to the very deep spectroscopy in the MUDF we can further test for the presence of a diffuse cool intragroup medium by stacking the spectra of background galaxies that lie behind the $z \approx 0.88$ group. We analyse four stacks: (A) 18 galaxies selected to have a S/N > 3 per wavelength channel in two spectral windows bracketing the wavelength of the $z \approx 0.88$ absorption (red ellipses in Fig. 11); (B) seven galaxies that are roughly cospatial with the distribution of the group galaxies (blue ellipses); (C) three galaxies which show Mg II absorption at $z \approx 0.88$ in their individual spectra (green ellipses); and (D) four galaxies lying between the two QSO sightlines and roughly aligned with the geometrical centre of the group (orange ellipses). Fo position of the group galaxies is shown by black dashed ellipses. The stacked spectra are shown in Fig. 12 as black lines, with 1σ uncertainty from bootstrap resampling shown in grey.

In stacks A and D we find non-detections with 2σ upper limits of $W_{2796} < 0.28 \, \text{Å}$ and $W_{2796} < 0.47 \, \text{Å}$ respectively. In stack B, which is restricted to the galaxies aligned with the two foreground sub-groups, we find a $\sim 3.5\sigma$ combined detection of the Mg II doublet with $W_{2796} = 0.61^{+0.22}_{-0.23} \, \text{Å}$, although with an $\approx 50 \, \mathrm{km \, s^{-1}}$ offset with respect to the absorber seen in the bright quasar sightline (red solid line). We checked by comparing the MUSE and UVES spectra of the quasars that this offset is real, and does not arise from
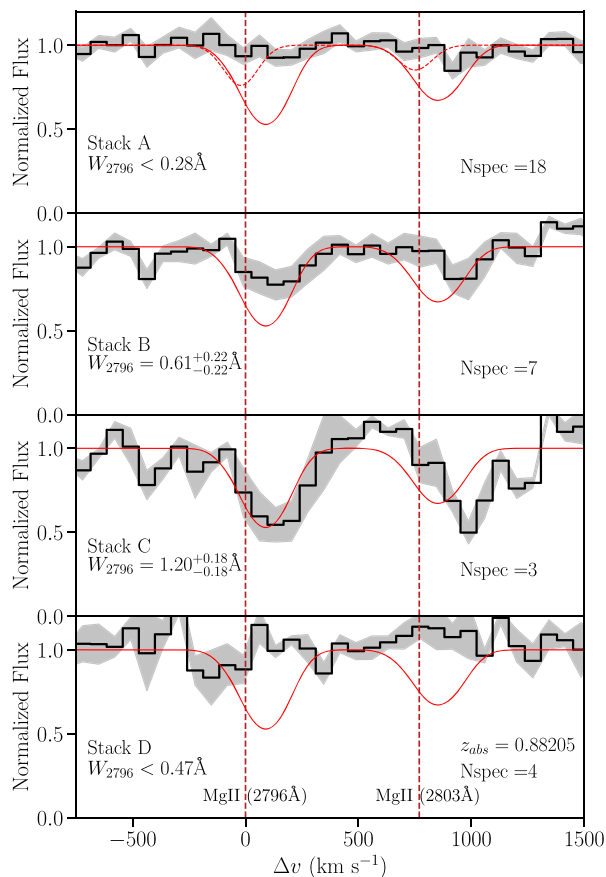
Figure 12. Stacked spectra (black) of MUDF background sightlines probing galaxies of the $z \sim 0.88$ group around the Mg II doublet. The panels from top to bottom refer to stacks A to D as described in the main text. The grey filled region shows the 1σ uncertainty from bootstrap resampling. The zero velocity is defined by the average redshift of the group ($z = 0.88205$), and the rest velocity of each transition in the Mg II doublet is shown by red vertical dashed lines. The red solid line shows the best fit model of the UVES spectrum of the QSO-SE convolved to match the MUSE spectral resolution, while the red dashed line in the top panel shows the best fit model for the QSO-NW spectrum.

mismatches in the wavelength calibration. Lastly, in stack C, which is composed of galaxies in which the absorption signal can be detected in individual spectra, this detection becomes even stronger with $W_{2796} = 1.20^{+0.24}_{-0.21}$ Å. Again, this result reinforces the idea that there exists a large cross-section of cool gas in close proximity to the group galaxies (stacks B and C), but that there is no dense and widespread cool gas that gives rise to strong absorption signal filling larger scales beyond the regions traced by galaxies themselves (stack A), or the region between the two sub-groups (stack D).

7 DISCUSSION

7.1 A high fraction of strong Mg II absorbers in galaxy groups

We performed a search for galaxy groups at $0.5 < z < 1.5$ in the MUDF, finding seven groups of at least three galaxies. From abundance matching we obtain a virial mass for these groups in the range $\log(M_h/M_\odot) \approx 11$–$13.5$, with virial radii in the range ≈ 100–200 kpc. Our most massive group includes 15 galaxies and

could evolve into a Virgo-like cluster of galaxies by $z = 0$ (Chiang, Overzier & Gebhardt 2013).

An independent search for cool gas absorbers, as traced by the Mg II doublet in the same redshift range, revealed five absorption systems in the high resolution spectrum of the brighter QSO-SE, and one system in the spectrum of the fainter QSO-NW. In total, of these six absorbers, five are at the same redshift as a galaxy group, a fraction of 83 per cent. For the only absorber not associated with a group, we found a galaxy within 300 km s^{-1} in velocity space. This galaxy is massive ($\log(M_*/M_\odot) = 10.51$), which corresponds to a dark matter halo mass of $\log(M_h/M_\odot) \approx 12.25$, following Moster et al. (2010). At this mass, it is very likely that the halo hosts several satellite galaxies which could be outside our survey footprint, so with spectroscopic data covering a larger area we might find this galaxy to be part of a group as well. Indeed, by looking at the absorption profiles in Fig. 9, this absorber looks kinematically complex, with several strong and narrow absorption components as found for the absorbers associated with galaxy groups.

Despite the alignment in redshift space between the group galaxies and the absorption profiles, it is difficult to unambiguously conclude whether we are observing gas in the intragroup medium, or whether absorption rises ultimately from the CGM of individual group members. Throughout our analysis, however, we have uncovered pieces of evidence that more closely support the latter scenario.

We have found that all the Mg II detections arise in groups with at least one galaxy closer than 150 kpc from the bright quasar line of sight, and the same is true for the single absorber in the faint quasar. Moreover, the group galaxies which are closer in redshift space to the absorbers are also closer in projection, and groups with a Mg II detection appear to host relatively massive galaxies that are expected to have intrinsically larger cross sections of cool gas in their CGM. Similarly, all the non-detections are associated with galaxies at larger distances from the sightline, or that are at lower mass (and hence likely have smaller cross sections) compared to the members of groups with a Mg II detection.

We have not found compelling evidence for the presence of a widespread intragroup medium producing strong absorption for two reasons. First, out of four Mg II systems associated with groups, only one system (at $z \approx 0.88$) is detected in the two sightlines, and the profiles are not very well correlated in velocity space. Secondly, when stacking galaxies in the background of this $z \approx 0.88$ group, a detection of Mg II in absorption emerges only when considering background galaxies in at small projected separations to the foreground ones. Altogether, these pieces of evidence suggest that the strong absorbers are associated mostly with the CGM of group galaxies. However, we do not rule out the presence of a homogeneous low-density intragroup medium which can give rise to weak absorption components.

This conclusion, however, does not rule out environmental effects from shaping the properties of the CGM of group members. Indeed, when considered by their equivalent width, group galaxies appear to host stronger Mg II absorbers compared to the general galaxy population. Several studies that have focused on samples of (relatively massive) galaxies probed by quasar sightlines, not selected according to their environment, have uncovered a clear anticorrelation between W and impact parameter d (Steidel et al. 1994; Chen et al. 2010). A similar trend seems to hold also in samples where background galaxies are used to probe foreground ones (Rubin et al. 2018a). In these samples, strong absorbers with equivalent width $W > 1$ Å are typically found at $d < 30$ kpc. Conversely, in our groups, strong systems are found at distances

$\approx 50 - 100$ kpc, despite the fact that we do not necessarily probe more massive galaxies than these previous studies (see Fig. 10).

While the most massive galaxies ($M_* \approx 10^{11}$ M$_\odot$) in samples from the literature are themselves likely members of groups, generally these samples are thought to be more representative of the field population. Indeed, using a light cone from the Henriques et al. (2015) semi-analytic model of galaxy formation, we find that for galaxies with a stellar mass in the range $10^{9.75} - 10^{10.25}$ M$_\odot$ and redshift $0.4 < z < 0.6$, a fraction of only 42 per cent live in groups as defined by our method, with this fraction reducing even further at lower stellar mass. Thus, the samples of Chen et al. (2010) and Rubin et al. (2018a), which in some cases extend down to 10^9 M$_\odot$, are representative of a more isolated population of galaxies compared to the sample of group galaxies studied in this work. Therefore, the difference in absorption strength at fixed impact parameter, combined with the complex kinematical profiles, imply that the group environment plays an active role in boosting the cross-section of cool gas present in the CGM of member galaxies.

This result, that emerges from a complete and systematic search of groups in the MUDF, is in line with previous findings from serendipitous discoveries of groups associated with Mg II absorbers. For instance, Whiting, Webster & Francis (2006) found at least five galaxies at the redshift of a $W = 2.5$ Å Mg II absorber. Similarly, Kacprzak, Murphy & Churchill (2010) found five low-mass galaxies associated with a $W = 1.8$ Å absorber. Nestor et al. (2011) found ultrastrong Mg II absorbers with $W = 3.6, 5.6$ Å in two systems associated with massive galaxy pairs, and lastly Gauthier (2013) found another very strong absorber with $W = 4.2$ Å in a group of three galaxies. These works found that the closest galaxy is at $d = 30 - 70$ kpc. In the work by Kacprzak et al. (2010) a galaxy is found to have a smaller impact parameter (17.4 kpc). However, from an analysis of the metallicity of the absorber and of the group galaxies, the authors concluded that the closest galaxy is not hosting the absorber, which is more likely to arise from tidal debris in the group environment. Bordoloi et al. (2011) found marginally more extended Mg II absorption profiles compared to a sample of more isolated galaxies, concluding that the absorbing gas is more likely to be associated to the individual galaxies rather than the intragroup medium. Nielsen et al. (2018) similarly found an enhanced equivalent width of Mg II absorbers in a sample of 29 galaxy groups with respect to an isolated galaxy sample. These authors have complemented these results with a kinematical analysis of the absorption profiles and concluded that the absorbers originate from an intragroup medium rather than from individual galaxies. However, it remains unclear if these sparse groups (having on average 2–3 members) are part of a virialized halo that is able to host a diffuse intragroup medium. Lastly, Bielby et al. (2017) studied the Mg II absorption profile associated to a low-mass group at $z \approx 0.28$ finding that the absorbing gas is likely to arise from multiple gas clouds orbiting in the group halo and giving rise to the intragroup medium.

7.2 The origin of enhanced cold gas in galaxy groups

We have uncovered evidence supporting a scenario in which, at fixed stellar mass, group galaxies have a larger cross-section of cool gas that gives rise to frequent and strong absorption systems. A question arises about what mechanisms may be responsible for this enhancement.

Several physical mechanisms might contribute to a larger cross-section of Mg II in group galaxies, including higher gas fractions for satellite galaxies in dense environments (Noble et al. 2017) or

stronger outflows from stellar winds due to enhanced star formation (McGee, Bower & Balogh 2014). There seems however to be no clear consensus on the relevance of these mechanisms in groups at $z \approx 1$ (Wetzel, Tinker & Conroy 2012; Fossati et al. 2017; Rudnick et al. 2017). Moreover we find it difficult to assess the contribution of these mechanisms with our own data. As we argue below, however, a prominent mechanism at play is likely to be gravitational interaction among group members.

It is well known that galaxy groups are the ideal environment to trigger gravitational interactions among members. Indeed, in more massive haloes (i.e. galaxy clusters), the higher velocity dispersion leads to shorter interaction times, with a reduced effect of tidal interactions on the gaseous and stellar structure of galaxies (see Boselli & Gavazzi 2006). Massive groups are therefore a sweet-spot in terms of richness and velocity dispersion for gravitational encounters to occur. For this reason, we argue that the evidence described above suggests that absorbers arise from gas once bound to the group galaxies (or their CGM), which has been stripped by tidal forces. This material, displaced from its original site, naturally boosts the cross-section of cool gas, leading to enhanced absorption at larger impact parameters compared to the field galaxies (Morris & van den Bergh 1994). These tails, gaseous bridges, and plumes have indeed been imaged in atomic and ionized gas within groups in the local Universe (Mihos et al. 2012; Rasmussen et al. 2012; Taylor et al. 2014; Fossati et al. 2019), where the denser components can stretch up to scales of hundreds of kpc. In this picture, the several kinematic components seen in the absorbers could be related to the chaotic orbits of the group galaxies during the stripping process, as seen for instance in the complex kinematic maps of galaxy encounters traced in emission with MUSE (Fossati et al. 2019).

This process would explain why a correlated detection of cool gas in both the MUDF quasars is a rare event. Given the distance of ~500 kpc between the two sightlines, a double detection requires either a very massive group that spans this distance with enough galaxies, a number of which is subject to some degree of gravitational perturbation. Alternatively, a special alignment of galaxies is required, as in the $z \sim 0.88$ group, which is composed of two subgroups that fortuitously align with the orientation of the two quasars.

The connection between enhanced Mg II absorption and a tidal stripping scenario is further reinforced by other works. For instance, Kacprzak et al. (2010), using the high-resolution of *HST* imaging data, found perturbed morphologies for the three brightest group galaxies, with tidal tails extending up to ~25 kpc. They conclude that these morphological features are suggestive of merger events or tidal stripping and that dense and cool stripped gas can host the observed Mg II absorber. More recently, Chen et al. (2019) studied the same group with deep MUSE observations. These data corroborated the results of Kacprzak et al. (2010) revealing a giant nebula of ionized gas contributing to the total mass and metal content of the intragroup medium. An accurate kinematical analysis showed that the Mg II absorber is indeed located in the stripped gas passing in front of the background quasar. These results point towards the presence of a multiphase medium (see also Bielby et al. 2017), and it is possible that the cool and ionized gas is gradually heated to the group virial temperature, contributing to the warm–hot intragroup medium.

8 SUMMARY AND CONCLUSIONS

In this work, we have presented the design, observations, and data reduction methodology for the MUDF survey, together with results from the cold gas content of galaxy groups at $0.5 < z < 1.5$. The MUDF survey is a 150 h (on source) large programme on the MUSE

instrument at the VLT that is observing a 1.5×1.2 arcmin^2 region of the sky characterized by the presence of two quasars at $z \approx 3.22$ separated by ≈ 60 arcsec. The MUSE data are also complemented by *HST* imaging programmes in the near-UV and in the near-IR, and by the deepest *HST* near-IR spectroscopic campaign in a single field. Deep high-resolution spectroscopy of the quasars is also being collected with the UVES instrument at the VLT. These rich data sets will enable us to reach several goals, including: an investigation into the connection between gas and galaxies reaching the low-mass regime at $z \sim 2-3$; a search for gas filaments of the cosmic web in emission; and a study of the build-up of the Hubble sequence with cosmic time with accurate information on the morphology, kinematics, gas budget, and star-formation history of galaxies.

In this paper, we have discussed in detail the survey design, the data reduction procedure, the extraction and validation of source catalogues, and the derivation of the physical properties of galaxies from the partial data set observed to date. As a first application, we investigated the galaxy environments in the MUDF, finding seven groups three or more members at $0.5 < z < 1.5$ covering a large range in inferred dark matter halo mass ($\log(M_h/M_\odot) \approx 11 - 13.5$). We explored the correlation between galaxies and galaxy groups with cold gas detected via Mg II absorption in the quasar sightlines. We found five absorption systems in the spectrum of the bright quasar and only one in the faint quasar spectrum. All but one of these systems are at the redshift of a galaxy group, while for the last one we find a massive galaxy at a small velocity separation, which we speculate could itself be a member of a group falling outside the MUDF footprint.

The absorbers have a complex velocity profile which we decompose into several Voigt components using a novel Bayesian technique. We find that, within a given group of galaxies, members that are close in velocity space to the absorber are also closer to the sightline in projection compared to the other group galaxies. Furthermore, through the analysis of correlated absorption in both quasar sightlines and via a tomographic map of one of the groups using background galaxies, we find no significant evidence of a widespread and homogeneous intragroup medium giving rise to a strong absorption signal. Altogether, these results suggest that the absorbers reside in (or are stripped from) the CGM of one or more galaxies within ≈ 100 kpc from the quasar sightline.

The strength of the absorption seen in groups is higher than what is typically found for more isolated galaxies at comparable impact parameters. This evidence, combined with previous examples in the literature of strong Mg II absorbers in group-like environments, suggests that the absorbers reside in gas once bound to individual galaxies (or their CGM) that has been stripped at larger radii, boosting the cross-section of Mg II. Gravitational interactions and tidal forces, in analogy with what is seen in nearby groups, are indeed effective in galaxy groups and obvious mechanisms to strip gas and stars from the galaxy discs, leading to the observed phenomenology.

So far, our analysis relied on deep MUSE data in a double quasar field. These data will soon be complemented by deep spectroscopic and imaging data from *HST*, extending the wavelength of our observations from the near-UV to the near-IR. These data will provide us with accurate redshifts for galaxies in the redshift desert ($1.5 < z < 3.0$), as well as strong constraints on the stellar mass and recent star-formation of galaxies down to low stellar mass. The approach of combining multiple quasar sightlines with complete galaxy surveys and an accurate reconstruction of the galaxy environment is critical for understanding the role of strong absorbers in the framework of how galaxies are fed with fresh gas. In forthcoming papers, we will study the impact of the group environment on the star-formation activity of galaxies, while extending this work to higher redshift.

REFERENCES

Abbott T. M. C. et al., 2018, ApJS, 239, 18
Akaike H., 1974, IEEE Trans. Autom. Control, 19, 716
Astropy Collaboration, 2013, A&A, 558, A33
Bacon R. et al., 2010, in McLean I. S., Ramsay S. K., Takami H., eds, Proc. SPIE Conf. Ser. Vol. 7735, Ground-based and Airborne Instrumentation for Astronomy III. SPIE, Bellingham, p. 773508
Bacon R. et al., 2017, A&A, 608, A1
Balogh M. et al., 2004, MNRAS, 348, 1355
Balogh M. L. et al., 2014, MNRAS, 443, 2679
Bergeron J., 1986, A&A, 155, L8
Berlind A. A. et al., 2006, ApJS, 167, 1
Bertin E., Arnouts S., 1996, A&AS, 117, 393
Bielby R., Crighton N. H. M., Fumagalli M., Morris S. L., Stott J. P., Tejos N., Cantalupo S., 2017, MNRAS, 468, 1373
Bordoloi R. et al., 2011, ApJ, 743, 10
Bordoloi R., Lilly S. J., Kacprzak G. G., Churchill C. W., 2014a, ApJ, 784, 108
Bordoloi R. et al., 2014b, ApJ, 796, 136
Borisova E. et al., 2016, ApJ, 831, 39
Boselli A., Gavazzi G., 2006, PASP, 118, 517
Bouché N. et al., 2010, ApJ, 718, 1001
Brammer G. B., van Dokkum P. G., Coppi P., 2008, ApJ, 686, 1503
Bruzual G., Charlot S., 2003, MNRAS, 344, 1000
Buchner J. et al., 2014, A&A, 564, A125

Byler N., Dalcanton J. J., Conroy C., Johnson B. D., Levesque E. M., Berg D. A., 2018, ApJ, 863, 14

Calzetti D., Armus L., Bohlin R. C., Kinney A. L., Koornneef J., Storchi-Bergmann T., 2000, ApJ, 533, 682

Cantalupo S. et al., 2019, MNRAS, 483, 5188

Chabrier G., 2003, PASP, 115, 763

Chen H.-W., Tinker J. L., 2008, ApJ, 687, 745

Chen H.-W., Helsby J. E., Gauthier J.-R., Shectman S. A., Thompson I. B., Tinker J. L., 2010, ApJ, 714, 1521

Chen H.-W., Boettcher E., Johnson S. D., Zahedy F. S., Rudie G. C., Cooksey K. L., Rauch M., Mulchaey J. S., 2019, ApJ, 878, L33

Chiang Y.-K., Overzier R., Gebhardt K., 2013, ApJ, 779, 127

Colbert J. W., Scarlata C., Teplitz H., Francis P., Palunas P., Williger G. M., Woodgate B., 2011, ApJ, 728, 59

Conroy C., Gunn J. E., White M., 2009, ApJ, 699, 486

Crighton N. H. M. et al., 2011, MNRAS, 414, 28

Cucciati O. et al., 2014, A&A, 565, A67

Cupani G. et al., 2016, in Chiozzi G., Guzman J. C., eds, Proc. SPIE Conf. Ser. Vol. 9913, Software and Cyberinfrastructure for Astronomy IV. SPIE, Bellingham, p. 99131T

D'Odorico V., Petitjean P., Cristiani S., 2002, A&A, 390, 13

Davé R., Finlator K., Oppenheimer B. D., 2012, MNRAS, 421, 98

Dekel A., Birnboim Y., 2006, MNRAS, 368, 2

Dekel A., Silk J., 1986, ApJ, 303, 39

Dekker H., D'Odorico S., Kaufer A., Delabre B., Kotzlowski H., 2000, in Iye M., Moorwood A. F., eds, Proc. SPIE Conf. Ser. Vol. 4008, Optical and IR Telescope Instrumentation and Detectors. SPIE, Bellingham, p. 534

Diener C. et al., 2013, ApJ, 765, 109

Dressler A., 1980, ApJ, 236, 351

Driver S. P. et al., 2011, MNRAS, 413, 971

Fazio G. G. et al., 2004, ApJS, 154, 10

Feroz F., Hobson M. P., 2008, MNRAS, 384, 449

Feroz F., Hobson M. P., Cameron E., Pettitt A. N., 2013, preprint (arXiv:1306.2144)

Finn C. W. et al., 2016, MNRAS, 460, 590

Fossati M. et al., 2017, ApJ, 835, 153

Fossati M. et al., 2018, A&A, 614, A57

Fossati M., Fumagalli M., Gavazzi G., Consolandi G., Boselli A., Yagi M., Sun M., Wilman D. J., 2019, MNRAS, 484, 2212

Francis P. J., Hewett P. C., 1993, AJ, 105, 1633

Fraternali F., Binney J. J., 2008, MNRAS, 386, 935

Fumagalli M., Cantalupo S., Dekel A., Morris S. L., O'Meara J. M., Prochaska J. X., Theuns T., 2016, MNRAS, 462, 1978

Fumagalli M., Haardt F., Theuns T., Morris S. L., Cantalupo S., Madau P., Fossati M., 2017a, MNRAS, 467, 4802

Fumagalli M. et al., 2017b, MNRAS, 471, 3686

Gaia Collaboration, 2018, A&A, 616, A1

Galametz A. et al., 2018, MNRAS, 475, 4148

Gallazzi A., Bell E. F., 2009, ApJS, 185, 253

Gauthier J.-R., 2013, MNRAS, 432, 1444

Giovanelli R., Haynes M. P., 1985, ApJ, 292, 404

Gunn J. E., Gott J. R., III, 1972, ApJ, 176, 1

Handley W. J., Hobson M. P., Lasenby A. N., 2015, MNRAS, 453, 4384

Henriques B. M. B., White S. D. M., Thomas P. A., Angulo R., Guo Q., Lemson G., Springel V., Overzier R., 2015, MNRAS, 451, 2663

Hinton S. R., Davis T. M., Lidman C., Glazebrook K., Lewis G. F., 2016, Astron. Comput., 15, 61

Hoyle B. et al., 2018, MNRAS, 478, 592

Huchra J. P., Geller M. J., 1982, ApJ, 257, 423

Kacprzak G. G., Churchill C. W., Steidel C. C., Murphy M. T., 2008, AJ, 135, 922

Kacprzak G. G., Murphy M. T., Churchill C. W., 2010, MNRAS, 406, 445

Kauffmann G., Nelson D., Ménard B., Zhu G., 2017, MNRAS, 468, 3737

Kereš D., Katz N., Weinberg D., Davé R., 2005, MNRAS, 363, 2

Klitsch A., Péroux C., Zwaan M. A., Smail I., Oteo I., Biggs A. D., Popping G., Swinbank A. M., 2018, MNRAS, 475, 492

Knobel C. et al., 2009, ApJ, 697, 1842

Knobel C. et al., 2012, ApJ, 753, 121

Kovač K. et al., 2010, ApJ, 708, 505

Kron R. G., 1980, ApJS, 43, 305

Lilly S. J., Carollo C. M., Pipino A., Renzini A., Peng Y., 2013, ApJ, 772, 119

Lofthouse E., Fumagalli M., Fossati M., O'Meara J., Murphy M. et al., 2019, MNRAS, submitted

Lusso E. et al., 2019, MNRAS, 485, L62

McGee S. L., Bower R. G., Balogh M. L., 2014, MNRAS, 442, L105

Mendel J. T., Simard L., Palmer M., Ellison S. L., Patton D. R., 2014, ApJS, 210, 3

Merlin E. et al., 2015, A&A, 582, A15

Mihos J. C., Keating K. M., Holley-Bockelmann K., Pisano D. J., Kassim N. E., 2012, ApJ, 761, 186

Momcheva I. G. et al., 2016, ApJS, 225, 27

Morrissey P. et al., 2018, ApJ, 864, 93

Morris S. L., van den Bergh S., 1994, ApJ, 427, 696

Moster B. P., Somerville R. S., Maulbetsch C., van den Bosch F. C., Macciò A. V., Naab T., Oser L., 2010, ApJ, 710, 903

Muzzin A. et al., 2013, ApJ, 777, 18

Nestor D. B., Johnson B. D., Wild V., Ménard B., Turnshek D. A., Rao S., Pettini M., 2011, MNRAS, 412, 1559

Nielsen N. M., Churchill C. W., Kacprzak G. G., Murphy M. T., Evans J. L., 2015, ApJ, 812, 83

Nielsen N. M., Kacprzak G. G., Pointon S. K., Churchill C. W., Murphy M. T., 2018, ApJ, 869, 153

Noble A. G. et al., 2017, ApJ, 842, L21

Oemler A., Jr., 1974, ApJ, 194, 1

Oppenheimer B. D., Davé R., Kereš D., Fardal M., Katz N., Kollmeier J. A., Weinberg D. H., 2010, MNRAS, 406, 2325

Peng Y.-j. et al., 2010, ApJ, 721, 193

Perlmutter S. et al., 1999, ApJ, 517, 565

Péroux C. et al., 2017, MNRAS, 464, 2053

Planck Collaboration XIII, 2016, A&A, 594, A13

Prochaska J. X., Weiner B., Chen H.-W., Mulchaey J., Cooksey K., 2011, ApJ, 740, 91

Rasmussen J. et al., 2012, ApJ, 747, 31

Rubin K. H. R., Weiner B. J., Koo D. C., Martin C. L., Prochaska J. X., Coil A. L., Newman J. A., 2010, ApJ, 719, 1503

Rubin K. H. R., Diamond-Stanic A. M., Coil A. L., Crighton N. H. M., Moustakas J., 2018a, ApJ, 853, 95

Rubin K. H. R., Diamond-Stanic A. M., Coil A. L., Crighton N. H. M., Stewart K. R., 2018b, ApJ, 868, 142

Rudie G. C. et al., 2012, ApJ, 750, 67

Rudnick G. et al., 2017, ApJ, 849, 27

Schaye J., Aguirre A., Kim T.-S., Theuns T., Rauch M., Sargent W. L. W., 2003, ApJ, 596, 768

Schroetter I. et al., 2016, ApJ, 833, 39

Scoville N. et al., 2007, ApJS, 172, 150

Sharma M., Theuns T., 2019, preprint (arXiv:e-print)

Springel V. et al., 2005, Nature, 435, 629

Steidel C. C., Dickinson M., Persson S. E., 1994, ApJ, 437, L75

Steidel C. C., Erb D. K., Shapley A. E., Pettini M., Reddy N., Bogosavljević M., Rudie G. C., Rakic O., 2010, ApJ, 717, 289

Stocke J. T., Keeney B. A., Danforth C. W., Shull J. M., Froning C. S., Green J. C., Penton S. V., Savage B. D., 2013, ApJ, 763, 148

Taylor R., Minchin R. F., Herbst H., Davies J. I., Rodriguez R., Vazquez C., 2014, MNRAS, 443, 2634

Tejos N. et al., 2014, MNRAS, 437, 2017

Tumlinson J. et al., 2013, ApJ, 777, 59

Tumlinson J., Peeples M. S., Werk J. K., 2017, ARA&A, 55, 389

Tummuangpak P., Bielby R. M., Shanks T., Theuns T., Crighton N. H. M., Francke H., Infante L., 2014, MNRAS, 442, 2094

Turner O. J. et al., 2017, MNRAS, 471, 1280

Turner M. L., Schaye J., Steidel C. C., Rudie G. C., Strom A. L., 2014, MNRAS, 445, 794

van de Voort F., Schaye J., Booth C. M., Haas M. R., Dalla Vecchia C., 2011, MNRAS, 414, 2458

van der Wel A. et al., 2014, ApJ, 788, 28

Weilbacher P. M. et al., 2014, in Manset N., Forshay P., eds, ASP Conf. Ser. Vol. 485, Astronomical Data Analysis Software and Systems XXIII. Astron. Soc. Pac., San Francisco, p.451

Werk J. K. et al., 2014, ApJ, 792, 8

Werk J. K. et al., 2016, ApJ, 833, 54

Werner M. W. et al., 2004, ApJS, 154, 1

Wetzel A. R., Tinker J. L., Conroy C., 2012, MNRAS, 424, 232

White S. D. M., Rees M. J., 1978, MNRAS, 183, 341

Whiting M. T., Webster R., Francis P., 2006, MNRAS, 368, 341

Wuyts S. et al., 2011, ApJ, 738, 106

Yang X., Mo H. J., van den Bosch F. C., Pasquali A., Li C., Barden M., 2007, ApJ, 671, 153

York D. G. et al., 2000, AJ, 120, 1579

SUPPORTING INFORMATION

Supplementary data are available at *MNRAS* online.

Table 1. The properties of the continuum sources in the MUDF extracted by SEXTRACTOR with S/N > 3.

Please note: Oxford University Press is not responsible for the content or functionality of any supporting materials supplied by the authors. Any queries (other than missing material) should be directed to the corresponding author for the article.

This paper has been typeset from a TEX/LATEX file prepared by the author.